Detecting aliasing and artifact free co-seismic and tsunamigenic ionospheric perturbations using GPS

M. Sithartha Muthu Vijayan[1,2]* and K. Shimna[1,2]

[1]Multi-Scale Modelling Programme (MSMP), CSIR Fourth Paradigm Institute (CSIR-4PI), Bangalore, India

[2]Academy of Scientific and Innovative Research (AcSIR), Ghaziabad, India

Corresponding author: M. Sithartha Muthu Vijayan (vijayan@csir4pi.in)

Key Points:

1. Nonuniform spatial sampling and polynomial misfits introduce aliasing and artifacts in ionospheric perturbations
2. Spatio-Periodic Leveling Algorithm (SPLA) is efficient in removing aliasing and artifacts
3. SPLA detects 50% more perturbations compare to conventional methods and increases SNR up to 149%
4. SPLA efficiently detects perturbations at low elevations and removes the need of elevation cut-off

Abstract

Ionospheric perturbations induced by tsunamis and earthquakes can be used for tsunami early warning and remote sensing of earthquakes, provided the perturbations are characterized properly to distinguish them from the ones caused by other sources. The ionospheric perturbations are increasingly being obtained from Global Positioning System (GPS) based Total Electron Content (TEC) measurements sampled at uniform time intervals. However, the sampling is not uniform in space. The nonuniform spatial sampling along the GPS satellite tracks introduces aliasing if it is not accounted while computing the ionospheric perturbations. All the methods hitherto used to detect the co-seismic and tsunamigenic ionospheric perturbations did not account the nonuniform spatial sampling while computing these perturbations. In addition, the residual approach used to obtain the perturbations by detrending the TEC time series using high-order polynomial fit introduces artifacts. These aliasing and artifacts corrupt amplitude, Signal-to-Noise Ratio (SNR), phase, and frequency of the ionospheric perturbations which are vital to distinguish the perturbations induced by tsunamis and earthquakes from the rest. We show that Spatio-Periodic Leveling Algorithm (SPLA) successfully removes such aliasing and artifacts. The efficiency of SPLA in removing the aliases and artifacts is validated under two simulated scenarios, and using GPS observations carried out during two natural disasters – the 2004 Indian Ocean tsunami and the 2015 Nepal-Gorkha earthquake. We, further, studied the severity of aliasing and artifacts on co-seismic and tsunamigenic perturbations by analyzing its characteristics employing SNR, spatiotemporal, and wavelet analyses. The results reveal that removal of aliasing and artifacts using SPLA i) increases the SNR up to ~149% compared to the residual method and ~39% compared to the differential method, ii) distinctly resolves signals from sharp static variations, and iii) detects 50% more co-seismic ionospheric perturbations and 25% more tsunami-induced ionospheric perturbations in the two events studied. Cross-correlation of the perturbation time series obtained using the residual method and SPLA reveals that aliasing and artifacts shift the time of occurrence

by -7.64 minutes to +4.21 minutes. Further, the results show that the SPLA efficiently detects the perturbations at low elevation angles, thereby removing the need of applying elevation cut-off and increasing the area of ionospheric exploration of a GPS receiver.

Key Words: ionosphere; ionospheric perturbations; GPS; tsunami; earthquake; spatio-periodic leveling algorithm

1 Introduction

Earthquakes and tsunamis killed more people than all other types of natural disasters, claiming globally around 884,000 lives between 1980 – 2014 (UNISDR et al., 2015). Among these two natural disasters, tsunamis were the most deadly with an average of 79 deaths for every 1,000 people affected, compared to four deaths per 1,000 in the case of earthquakes (UNISDR et al., 2015). This makes tsunamis almost twenty times more deadly than earthquakes. As there is no mechanism exists at present to forecast or predict earthquakes and tsunamis, timely detection and early warning are the only alternatives to reduce the loss of lives caused by these disasters. Ionospheric studies carried out for the last two decades show that monitoring ionospheric perturbation induced by earthquakes (CIP – Co-Seismic Ionospheric Perturbations) and tsunamis (TIP – Tsunami induced Ionospheric Perturbation) using Global Positioning System (GPS) is a promising tool for the timely detection and early warning (For example, Astafyeva, 2019, Bagiya et al. 2017, Catherine et al., 2015, Jin et al., 2015, Occhipinti et al., 2013, Manta et al., 2020). Further, detection of ionospheric perturbations induced by earthquakes and Rayleigh waves showed the possibilities of ionospheric remote sensing of earthquakes (Ducic et al., 2003, Occhipinti, 2015) and CIPs detected over the epicentral area was found to be useful to determine the seismic source structure and rupture dynamics of the seismic fault (Astafyeva and Shults, 2019, Jin et al., 2015, Occhipinti, 2015). In addition, studying ionospheric perturbations caused by atmospheric events such as tropospheric convections (Azeem and Barlage, 2018), cyclones (Kong et al., 2018), and stratospheric gravity waves (Hoffmann et al., 2018) are also gaining interest among the researchers apart from the popular use of the ionospheric perturbations to study the geomagnetic storms (Prikryl et al., 2013, Cherniak et al., 2015). As far as earthquake studies are concerned, seismometers, strong-motion accelerometers and high-rate GNSS ground displacement observations are providing reliable information (Bock et al., 2011, Havskov and Alguacil, 2004). However, they are limited to land as the observations are predominantly terrestrial. In this scenario, CIPs detected using GPS can

be supplemental to seismic observations by providing information over both land and ocean (Occhipinti, 2015). However, distinguishing the ionospheric perturbations associated with earthquakes and tsunamis from the rest is essential to reap the complete benefits of GPS based ionospheric observations for seismic and tsunami studies. Distinguishing the ionospheric perturbations associated with various events from one another is achieved based on the characteristics of the perturbations, namely amplitude, velocity, frequency, and phase. However, accurate detection of the ionospheric perturbations and determining its characteristics fundamentally depends on the methodology employed to derive the perturbations from GPS based Total Electron Content (TEC) measurements (Shimna and Vijayan, 2018; 2020).

Ionospheric perturbations computed hitherto, using GPS based TEC observations sampled at uniform time intervals, implicitly assumed uniform spatial sampling. In reality, the distance between consecutive sampling locations or Ionospheric Pierce Points (IPP) is positioned at nonuniform intervals along the tracks of GPS satellites traced by ground-based GPS receivers. This leads to nonuniform spatial sampling of TEC along the satellite track. Eventually, this unaccounted nonuniform spatial sampling introduces a false spatiotemporal gradient (Fig. 1). These false spatiotemporal gradients will get amalgamated with the ionospheric perturbations and cause signal aliasing (Shimna and Vijayan 2020). Such aliasing could mislead detection and characterization of the ionospheric perturbations. Further, the distance between adjacent IPPs (inter-IPP distances) are nonlinear in time due to the nonuniform spatial sampling and, in general, it is big at low elevations and small at high elevations (Shimna and Vijayan 2020). Generally, the high aliasings at low elevation angles are attributed to elevation-dependent errors, like multi-path. The errors associated with the low elevation observations are alleviated, conventionally, by applying elevation cut-offs. However, discarding the low elevation observations is not a viable solution, particularly, for monitoring the ionospheric perturbations caused by earthquakes (Thomas et al., 2018) and tsunamis (Artru et al. 2005). Low elevation observations are vital to detect TIPs generated by tsunamis

propagating in the deep ocean using onshore GPS receivers. Hence, discarding low elevation observations limits the utility of GPS based ionospheric observations for tsunami and earthquake early warning. In addition, the residual approach used in many studies (for example, Astefyeva et al., 2009; Hickey et al., 2009; Rolland et al., 2011; Tsugawa et al., 2011; Jin et al. 2015; Komjathy et al., 2016; Savastano et al., 2017) in which the perturbation is computed by detrending the TEC time series using a high-order polynomial. Usage of single high-order polynomial across the TEC time series introduce severe artifacts in the ionospheric perturbations (refer section 2.2).

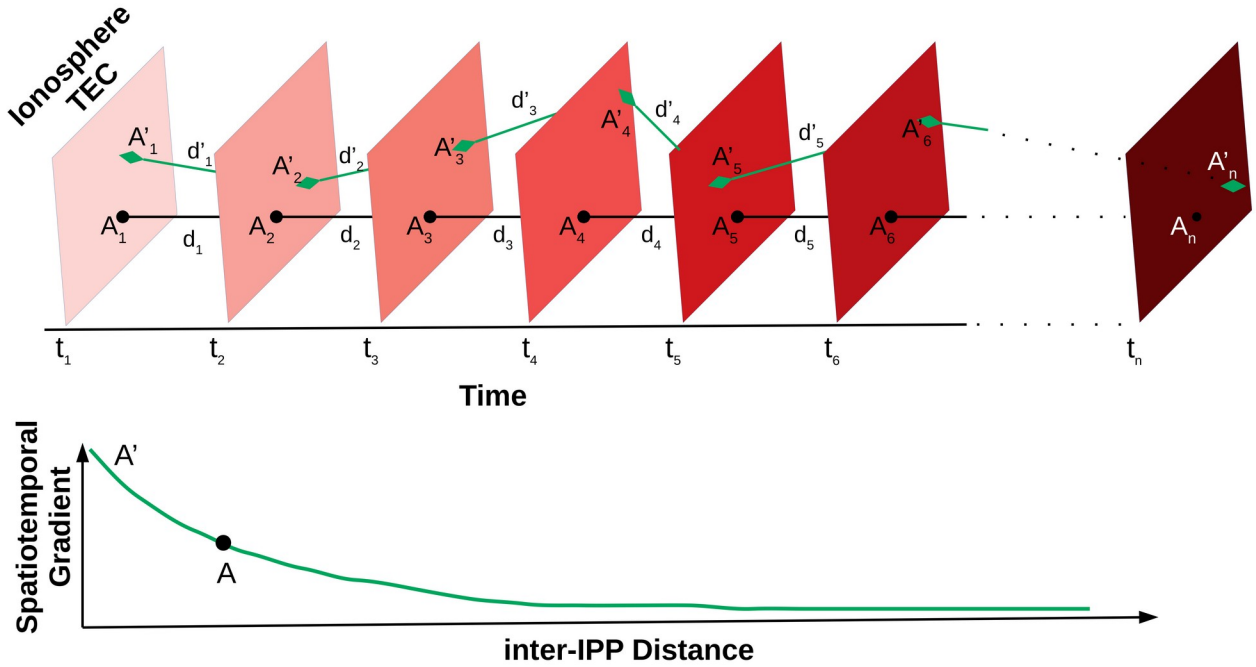

Figure 1: *Impact of nonuniform spatial sampling – schematic representation (not to scale). (Top) Spatially homogeneous ionosphere at times t_1 to t_n. Increase in the intensity of the color represents increasing concentration of TEC at a constant rate. TEC is sampled along track A at IPPs (black dots marked as A_1 to A_n) placed at uniform interval of time and space. Along the track A' the TEC is sampled (green diamonds marked as A'_1 to A'_n) at nonuniform spatial intervals and uniform time intervals. Inter-IPP distances along the track A ($d_1=d_2=d_3...=d_n=d$) are uniform; but along the track A' ($d'_1 \neq d'_2 \neq d'_3 \ldots \neq d'_n$) are nonuniform. (Bottom) Spatiotemporal Gradient (STG) along the track A (black) and A' (green) is shown as a function of inter-IPP distances (not to scale). STG = $\delta TEC/(dt \times dr)$ where δTEC is difference in TEC between two consecutive sampling points, dt is temporal sampling interval which is constant here, and dr is distance between the two adjacent sampling points.*

Considering the growing importance of ionospheric perturbations forced from below-the-ionosphere and its multifaceted applications, the accurate detection of ionospheric perturbations and robust determination of its characteristics using GPS are essential. However, to the best of our

knowledge, there is no study available in the published literature analyzing the aliases, artifacts, and methodology dependent errors in computing the ionospheric perturbations using GPS. In this study, for the first time, we analyze the aliases and artifacts present in the tsunami and earthquake induced ionospheric perturbations obtained using conventional methods, and show that adopting Spatio-Periodic Leveling Algorithm (SPLA) proposed by Shimna and Vijayan (2020) is efficient in obtaining aliasing and artifact free TIPs and CIPs irrespective of the elevation angles. We also demonstrate that SPLA removes the necessity of applying elevation cut-offs.

We use differential and residual methods to demonstrate the impact of aliasing and artifacts for brevity, though the problem of aliasing and artifacts are common to all the conventional methods including the ones which directly filters the TIP (Manta et al., 2020) or CIP from the TEC time series using a frequency filter. Further, we validate the efficiency of SPLA by testing the algorithm under two theoretically simulated scenarios (section 5), and using GPS observations carried out during the 2004 Indian Ocean tsunami and 2015 Nepal-Gorkha earthquake (section 6). In addition, we quantify improvement in the characteristics of the TIPs and CIPs (viz. Phase, frequency, and Signal-to-Noise Ratio (SNR)) upon removing aliases and artifacts caused by the nonuniform spatial sampling (section 7).

2. Conventional methods and its limitations

2.1 Differential method

Ionospheric perturbations computed by numerically differentiating the TEC between two successive epochs is known as differential TEC (dTEC) (Liu et al. 2004, 2006 and Catherine et al. 2015). This method is widely used to study the traveling ionospheric perturbations caused by forcing from below-the-ionosphere like tsunami, earthquakes, volcanic eruptions, cyclones, rocket launching, nuclear detonation, etc.

$$dTEC_R^S(t) = \frac{vTEC_R^S(t+1) - vTEC_R^S(t)}{\Delta t} \quad (1)$$

where $vTEC_R^S(t)$ is leveled vertical TEC along the ray path of a Satellite(S)-Receiver(R) pair at epoch *t,* and Δt is time difference between the two consecutive epochs.

$$vTEC = sTEC \times \cos(\zeta) \quad -(2)$$

where $\zeta = \sin^{-1}\left(\frac{R_e}{R_e + h_{max}} \cos\theta\right)$ and

$$sTEC = TEC_\phi + \langle TEC_p - TEC_\phi \rangle_{arc}$$

Where θ is elevation of satellite; sTEC is leveled slant TEC; TEC_ϕ and TEC_P are TEC computed from phase and code measurements, respectively; R_e is radius of the Earth and h_{max} is ionospheric shell height.

The sTEC along the ray path of satellite-receiver link from ground based GPS observations were computed using the software "IONODETECT" developed at CSIR-4PI (Vijayan et al., 2013; Catherine et al., 2015). IONODETECT computes sTEC by carrying out phase leveling along the phase connected arc for each satellite-receiver link using both code and phase measurements to remove carrier phase ambiguity. Further, the effect of slant ray path is corrected by mapping the sTEC to vertical TEC (vTEC), by assuming a single-layer model (Astafyeva et al., 2015; Jakowski and Hoque, 2019) where the ionosphere is approximated by a thin shell with a maximum ionization at a height of 350 km (Rao et al., 2006). The dTEC is measured in TECU s^{-1} (1 TECU = 10^{16} electrons/m^2).

In this method, the time-varying distance between the successive IPPs (or sampling points) are not accounted while computing the dTEC (Eq. 1). The unaccounted inter-IPP distances alter amplitude of the detected perturbation and alias as signal (Artru et al., 2005). Removing such signal aliases, manually, would be a laborious and time consuming process. In order to alleviate this problem, Galvan et al. (2011) introduced a residual method in which the ionospheric perturbations are obtained as residual TEC (rTEC) by detrending the regular characteristic variations of TEC along the IPP track formed by satellite-receiver link.

2.2 Residual method

The residual method is used in many seismo-ionopsheric and tsunami-ionospheric studies as an alternative to the differential method (Astafyeva et al., 2009; Galvan et al., 2011; Tsugawa et al., 2011; Jin et al., 2015). In this method, ionospheric perturbations, represented as a residual TEC (rTEC), is obtained by subtracting a high order polynomial fitted to the TEC time series from the observed TEC values.

$$rTEC = vTEC - P_t \quad (3)$$

where P_t is the high order polynomial representing the trend of vTEC time series along the IPP track formed by satellite-receiver link. In this work, we employ a 10^{th} order polynomial, following Galvan et al. (2011), to compute the trend along the arc.

The high-order polynomial is expected to represent the regular characteristic variations of TEC. However, the order cannot be too high because it would introduce additional variations in the residuals (Galvan et al., 2011). Hence, polynomials of varying degrees need to be applied for several cases and then a polynomial that could fit reasonably should be selected to represent the trend of each event-specific LoS-TEC time series. This makes the selection of a suitable polynomial subjective. Besides, an order of the polynomial is assumed to be uniform across LoS-TEC of all receiver-satellite pairs for ease of automation, especially, on computing rTEC in the case of dense networks of GPS receivers like the one in Japan (Galvan et al. 2011). This arbitrariness in the selection of the polynomial will allow the errors associated with the misfits to creep into the residual time series (rTEC) as signal aliasing and artifact. Further, severe misfits can lead to complete failure in detecting the perturbations. The post-processing of rTEC to remove the artifacts and aliasing will be complex and eventually leads to erroneous inferences. Moreover, the subjective selection of high order polynomial limits the use of the residual method for monitoring the perturbations in real-time.

Apart from differential and residual methods, methods like variometric approach (e.g. VARION – Variometric Approach for Real-Time Ionosphere Observation proposed by Savastano et al. (2017)) use both differential and residual approaches together for real-time detection of TIPs. VARION uses 8th order polynomial to fit the differential TEC time series, subtract the differential TEC from polynomial fit and represents the residuals as the variation due to a TID perturbation (see Savastano et al. (2017) for further details). In such cases, the obtained ionospheric perturbations will be affected by both aliasing and artifacts.

3. Algorithm to remove aliasing and artifacts: Spatio-Periodic Leveling Algorithm (SPLA)

To address the problem of aliasing in detecting ionospheric perturbations caused by geomagnetic storms and to compute the ionospheric perturbations free of signal aliasing, Shimna and Vijayan (2020) proposed an algorithm called Spatio-Periodic Leveling (SPLA). They also demonstrated that the SPLA is efficient in removing amplitude aliasing, particularly from low elevation observations, and thereby removes the need of applying elevation cut-off (Shimna and Vijayan, 2020). In this study, we show that the SPLA is also efficient in removing artifacts and inconsistencies, caused by polynomial misfits and elevation dependent slant ray path, from CIPs and TIPs in addition to removing the aliasing.

In SPLA, ionospheric perturbations are computed as gradient Rate of TEC (gROT) following a three-step process (Shimna and Vijayan, 2020):

Step 1: Impact of slant ray path is removed by converting the leveled sTEC into vTEC along a leveled phase connected arc (Eq. 2). The *vTEC* at a given time *t* is mapped to the location of IPP. The location of IPP (Φ_I, Λ_I) is computed using elevation (θ) and azimuth (ψ) angles subtended by the receiver R while tracking the satellite S. (Klobuchar, 1987).

Geographic latitude of IPP is

$$\Phi_I = asin\left(\sin\Phi_0\cos\alpha + \cos\Phi_0\sin\alpha\cos\psi\right) \quad -(4)$$

where α is Earth angle $\alpha = 90 - \theta - \zeta$, and Φ_0 is latitude of the GPS receiver.

Geographic longitude of IPP is

$$\Lambda_I = \Lambda_0 + asin\left(\frac{\sin\alpha\sin\psi}{\cos\Phi_I}\right) \quad -(5)$$

where ψ is azimuth angle; and Λ_0 is longitude of the GPS receiver.

Step 2: Computing rate of change of vTEC between two consecutive IPPs separated by an observational epoch (Δt) (Eq. 1).

Step 3: Removing the influence of inter-IPP distance (Δd) from the rate of change of vTEC and computing the spatiotemporal gradient at regular spatiotemporal intervals

$$gROT_R^S(t) = \frac{vTEC_R^S(t+1) - vTEC_R^S(t)}{\Delta d\,\Delta t} \quad -(6)$$

where R is receiver, S is satellite tracked by the receiver R, gROT is spatiotemporal gradient measured in TECU km^{-1} s^{-1} and Δd is inter-IPP distance.

Inter-IPP distance, Δd between two consecutive IPPs on a thin-shell ionosphere at a height of 350 km is

$$\Delta d = \left[R_e + h_{max}\right] \times acos\left(\sin\Phi_{I_1}\sin\Phi_{I_2} + \cos\Phi_{I_1}\cos\Phi_{I_2}\cos\Delta\Lambda\right) - (7)$$

where $\Delta\Lambda = \Lambda_{I_1} - \Lambda_{I_2}$; R_e is Radius of the Earth, h_{max} is ionospheric shell height. Δd, R_e and h_{max} are in km.

4. Filtering and Normalization

In order to filter the ionospheric perturbations associated with earthquake and tsunami, the estimated dTEC, rTEC and gROT are filtered using zero-phase bidirectional band-pass

(butterworth) filter with a pass band of 1.67 to 16 mHz (1-10 minute period) (Catherine et al, 2015) and 0.5 to 5 mHz (3.3 – 33.3 minute) (Galvan et al, 2011), respectively. The filtered dTEC, rTEC and gROT are normalized using Z-score normalization for inter-comparison as the three parameters are measured in different units.

$$Z = \frac{x - \mu}{\sigma} \text{ - (8)}$$

Where Z is the normalized dTEC or rTEC or gROT, x is filtered dTEC or rTEC or gROT, μ is mean of x, and σ is the standard deviation. The mean (μ) and standard deviation (σ) of dTEC, rTEC, and gROT are computed for each satellite-PRN time series.

In the following sections, we show that adopting the SPLA removes aliasing and artifacts from TIPs and CIPs using the normalized dTEC, rTEC and gROT.

5. Efficiency of SPLA: Theoretical validation

Efficiency of SPLA in detecting ionospheric disturbances without amplitude aliasing during a geomagnetic storm was theoretically validated by Shimna and Vijayan (2020). In this study, we first theoretically test the efficiency of SPLA in detecting aliasing and artifact free TIPs and CIPs over the conventional methods under two simulated scenarios and then using observational data sets. In the first scenario, the ability to detect sharp static variations was tested on a synthetic TEC time series added with step functions. In the second scenario, power of resolving the sharp static variations from the perturbations of comparable amplitude was tested using a synthetic TEC time series superimposed with both sharp static variations and a simulated perturbation.

The synthetic TEC was obtained by modeling the TEC using International Reference Ionosphere model IRI-2012 (Bilitza et al., 2014) at every IPP (IRI-TEC) along the satellite track traced by GPS satellite PRN04 observed at a uniform interval of 30 seconds from Hyderabad GPS station (HYDE) on 1st December 2004 from 06:52 UT to 13:22 UT (Fig. 2. Top-left). The satellite

track will be represented throughout this paper by PRN (Psuedo Random Noise) number of the GPS satellite prefixed with four letter GPS station code from where the GPS satellite was observed, for example, HYDE04.

5.1 Scenario – 1

In the first scenario, we introduced two Heaviside step functions (ς_H) with an interval of 60 seconds into the synthetic HYDE04 IRI-TEC at 7:48 UT with an amplitude of 0.3 and 0.5 TECU to test the efficiency of the three methods in detecting sharp static variations.

$$TEC_s(t) = TEC_s(t) + \varsigma_H(t) \quad -(9)$$

$$\varsigma_H(t) = A_s \times H[n];\ H[n] = \begin{cases} 0, n < t, \\ 1, n \geq t, \end{cases} \quad -(10)$$

where TEC_s is synthetic IRI-TEC along HYDE04, $H[n]$ is Heaviside step function, t is time and A_s is amplitude of the step function in TECU.

Residual method, differential method and SPLA were employed to detect the simulated sharp static variations added to the synthetic TEC_s (Fig. 2, Top-middle). The efficiency of detecting ionospheric sharp static variations by these three methods was assessed by analyzing the rTEC, dTEC and gROT using a Continuous Wavelet Transform (CWT) described by Grinsted et al. (2004). CWTs with (Fig. 2, middle) and without (Fig. 2, left) sharp static variations show that gROT and dTEC precisely detect the sharp static variations. However, CWT of rTEC shows that the residual method identifies the sharp static variation akin to ionospheric perturbation spread out for a long duration (7.5 UT to 11 UT). Furthermore, frequencies of static variations detected by the residual method fall within the characteristic frequency band of acoustic and acoustic gravity wave induced ionospheric perturbations. Such sharp static variations can normally occur as observational errors associated with undetected loss of locks, cycle slips, or scintillation.

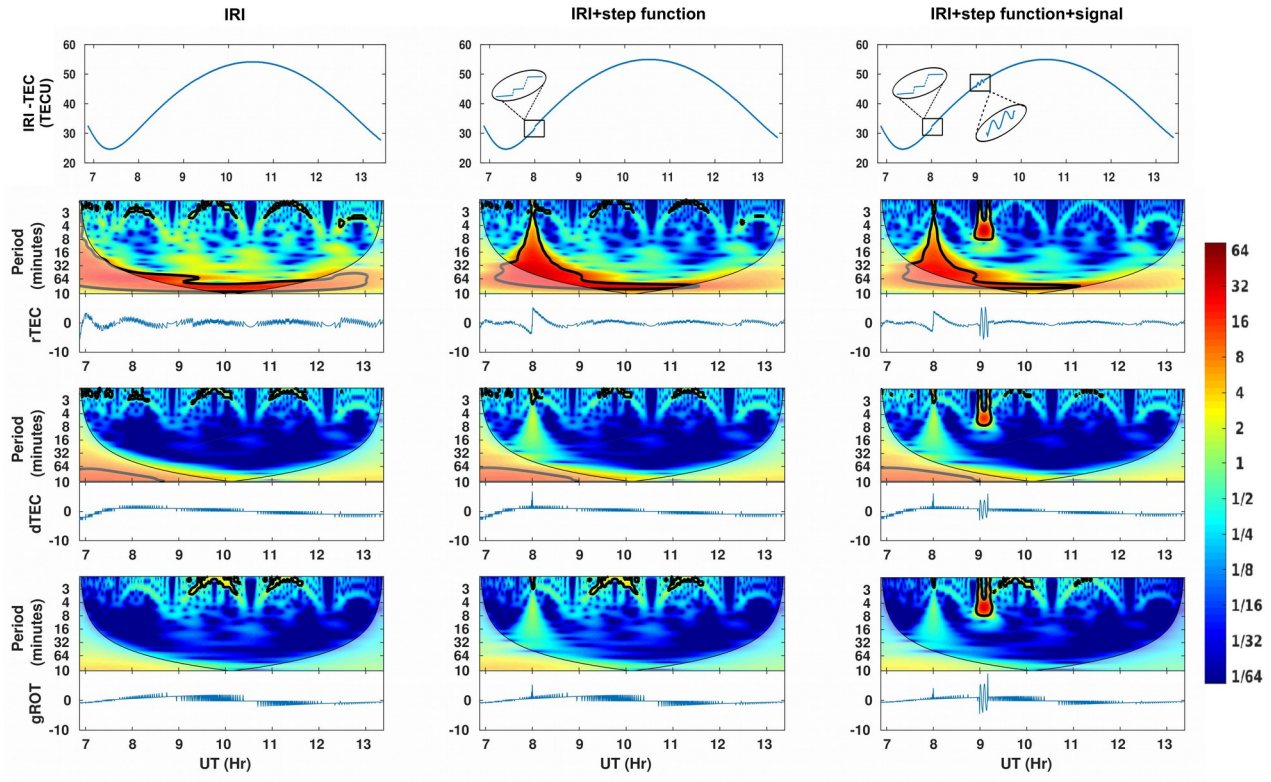

Figure 2: *(Top row) Time series of IRI-TEC (left), TEC synthesized for first (middle) and second scenario (right). Inlets show magnified portion of the sharp static variations and simulated perturbation. (2nd, 3rd and 4th rows) Continuous wavelet transforms and corresponding time series of normalized rTEC, dTEC and gROT.*

5.2 Scenario – 2

In the second scenario, the ionospheric perturbation of the form $y(\Phi_I, \Lambda_I, t)$ moving with an amplitude of 0.6 TECU and velocity of 1 km/s were simulated by considering a frequency of 3 mHz for a duration of 10 minutes. The frequency of 3mHz was selected to represent the perturbations common to both CIPs and TIPs

$$y(\Phi_I, \Lambda_I, t) = A\sin(k_1\Phi_I + k_2\Lambda_I - \omega t) \quad (11)$$

where Φ_I and Λ_I are latitude and longitude of IPPs, A is amplitude, $k_1 = k\cos(\Theta)$, $k_2 = k\sin(\Theta)$, k is wave number, ω is angular frequency, t is time and Θ is propagation angle.

The ionospheric perturbations thus simulated were superimposed on the step function introduced IRI-TEC synthesized in the second scenario to assess the resolving power of SPLA (Fig. 2, top-right).

Residual method, differential method, and SPLA were employed to extract the simulated perturbations from the newly synthesized IRI-TEC. The perturbations extracted by employing residual (rTEC), differential (dTEC) and SPLA (gROT) methods were analyzed using CWT (Fig. 2, right).

The results of CWT analysis manifest that the SPLA and differential method are better than the residual method in resolving the signal from sharp static variations (Fig. 2, right). Further, the residual method fails completely to resolve the sharp static variations from the simulated signal (Fig. 2, right).

The theoretical efficiency tests carried out considering the two scenarios clearly establish that the SPLA is superior in (i) detecting sharp static variations and (ii) resolving the signal from sharp static variations which normally occur due to undetected cycle-slips or scintillation in TEC time series.

6. Efficiency of SPLA: Observational Validation

SPLA is validated by computing ionospheric perturbations from GPS observations carried out during the two different geophysical events, viz. (i) 26th December 2004 Sumatra-Andaman Tsunami, and (ii) 25th April 2015 Nepal-Gorkha earthquake. The perturbations occurred during these events were also computed using residual, and differential methods for comparison. Efficiency of SPLA in removing the aliases is validated by comparing the normalized rTEC, and dTEC with gROT, and by computing the magnitude of aliasing.

6.1 Data description

GPS observations carried out at 15 GPS stations from 25th to 27th December 2004 with a sampling interval of 30 s were used to study the TIPs associated with the 26th December 2004 Indian ocean tsunami. Similarly, the Nepal GPS network data observed with a sampling interval of 15 s at 19 GPS stations on 24th-26th April 2015 were used to derive the CIPs induced by the 25th April 2015 Nepal-Gorkha earthquake. IGS and Nepal GPS stations data were downloaded from UNAVCO (ftp://data-out.unavco.org/pub/rinex/obs/) data repository.

6.2 Geometry of the observation

The Indian Ocean tsunami-induced TIPs were analyzed using the TIPs obtained at ~870,000 IPPs formed by all the GPS stations covering the Indian ocean from 40^{o} E to 130^{o} E and 50^{o} S to 50^{o} N (Fig. 3). Similarly, Nepal earthquake near-field CIP analysis was carried out at ~950,000 IPPs over the Himalayan region from 80^{o} E to 92^{o} E and 25^{o} N to 31^{o} N (Fig. 4).

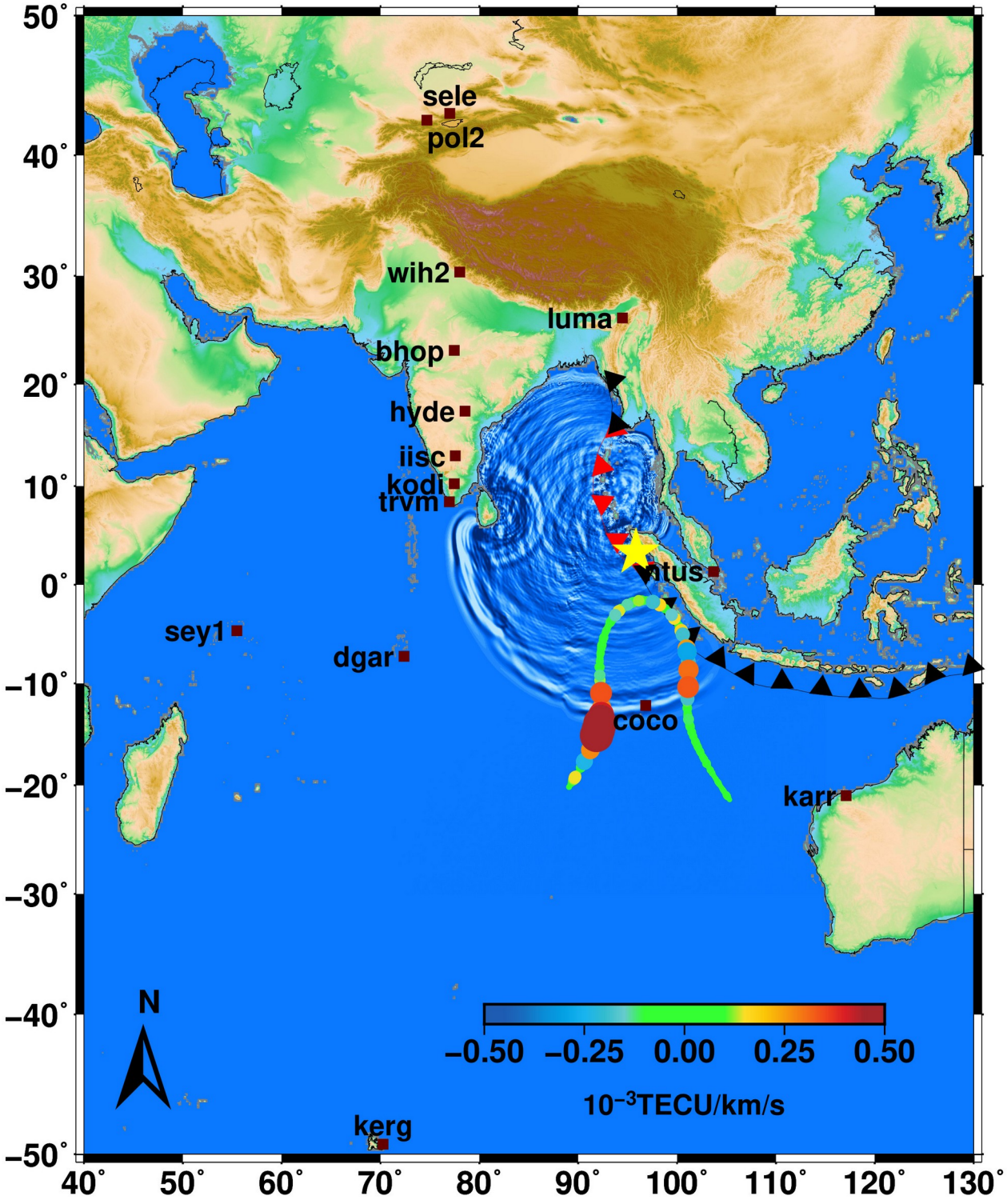

***Figure 3**: Location of GPS stations used to observe the TIP. Numerically simulated tsunami waves propagating at 3.5 UT and TIP observed along COCO07 (3 UT to 13 UT) is shown in the background. Yellow star represents epicenter of tsunamigenic Mw9.2 Sumatra-Andaman earthquake.*

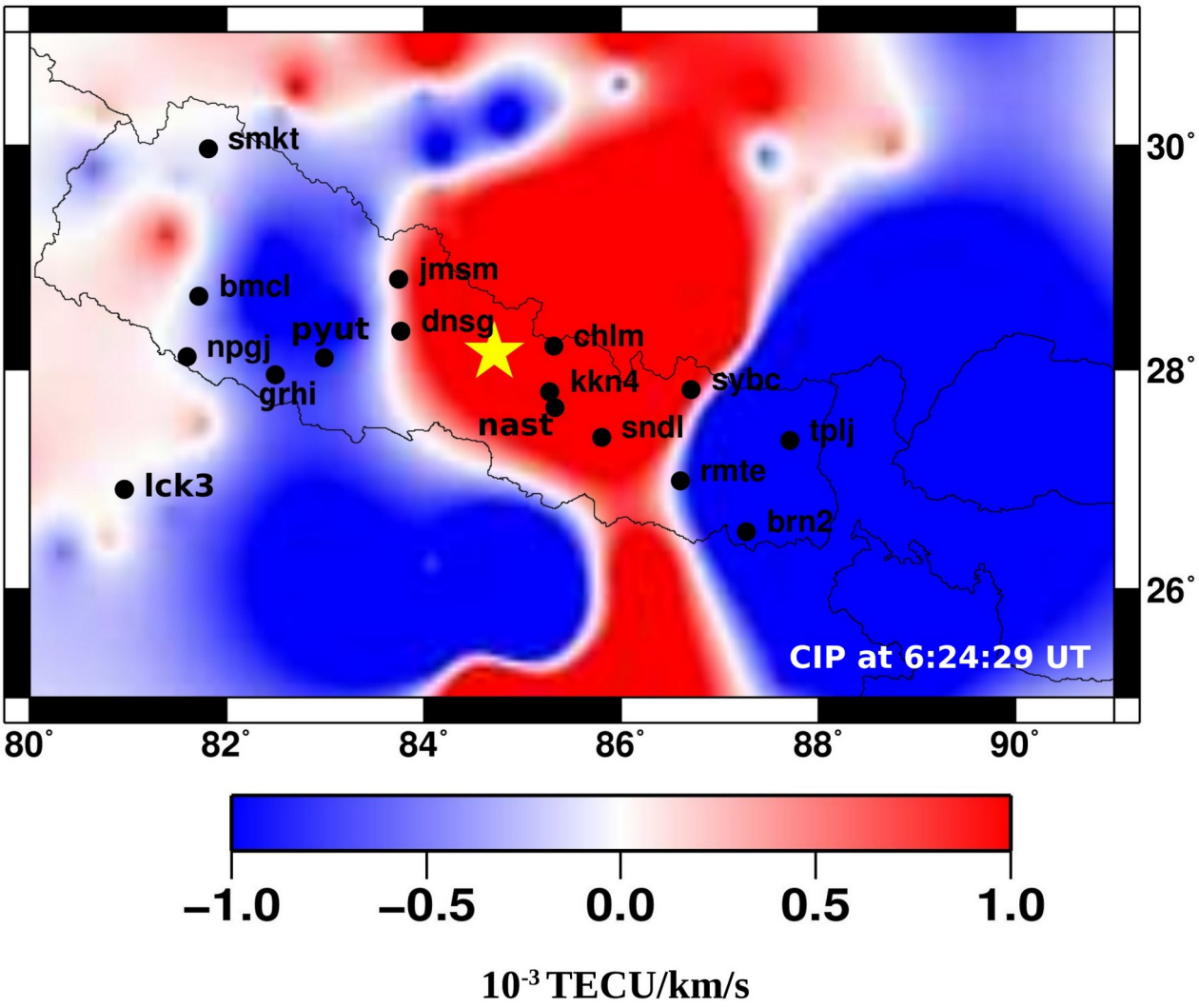

Figure 4: *Location of GPS stations used to obtain CIPs are overlaid on spatially interpolated CIPs detected at 6:24:29 UT on 25th April 2015 around the epicentral area of Mw7.8 Nepal-Gorkha earthquake. Yellow star represents epicenter*

6.3 Observational environment

The giant Sumatra-Andaman earthquake of magnitude Mw 9.1 occurred off the west coast of Sumatra at 00:58:52 UT on 26th December 2004 triggered the most devastating tsunami in the Indian Ocean (Lay et al., 2005). Acoustic gravity waves generated by the tsunami perturbed the ionosphere when the geomagnetic condition was weak (Liu et al., 2006) . The tsunami wave-field was simulated using COMCOT (Liu et al., 1998; Wang and Liu, 2006) by modeling the ocean surface displacement at six fault segments (Hebert et al., 2007) to identify the TIPs induced by the

tsunami (Fig. 3). TIPs associated with the simulated tsunami (time lag of ~25 minutes corresponds to vertical propagation of acoustic gravity waves) are considered in this analysis.

Similarly, the Nepal-Gorkha earthquake (Fig. 4) occurred on 25th April 2015 at 06:11:26 UTC with the magnitude of Mw 7.8 had ruptured around 160 km with a duration of 55 s (Fan et al., 2015) disturbed the ionosphere and generated CIPs under extremely quiet geomagnetic conditions (Kong et al., 2018). CIPs obtained in the near field of the earthquake are considered in this analysis.

6.4 Detecting aliasing and artifacts free TIPs

Aliases and artifacts in TIPs computed using differential and residual methods and its removal by SPLA are illustrated here using observations along the track of COCO07, COCO17, IISC26, and HYDE29 (Fig. 5, 6, 7 and 8). In all the four cases, the TIPs were detected at low elevations which are conventionally discarded to avoid the errors associated with multipath, and slant ray paths. But, the coincidence in time and location of the perturbations with the simulated tsunamis (Fig. 7, and 8) ensures that the perturbations obtained from GPS-TEC observations are TIPs associated with the Indian Ocean tsunami. Moreover, in the case of COCO07 (Fig. 5) and COCO17 (Fig. 6) elevation varies only from 5°-35° during 11 hours of continuous observation. For example, applying a 30° elevation cut-off in such cases leads to omission of the observations almost in its entirety. Such omissions will eventually lead to missing onshore detection of tsunamis propagating in the open ocean. This emphasizes the importance of removing errors associated with low elevation observations from the TIPs.

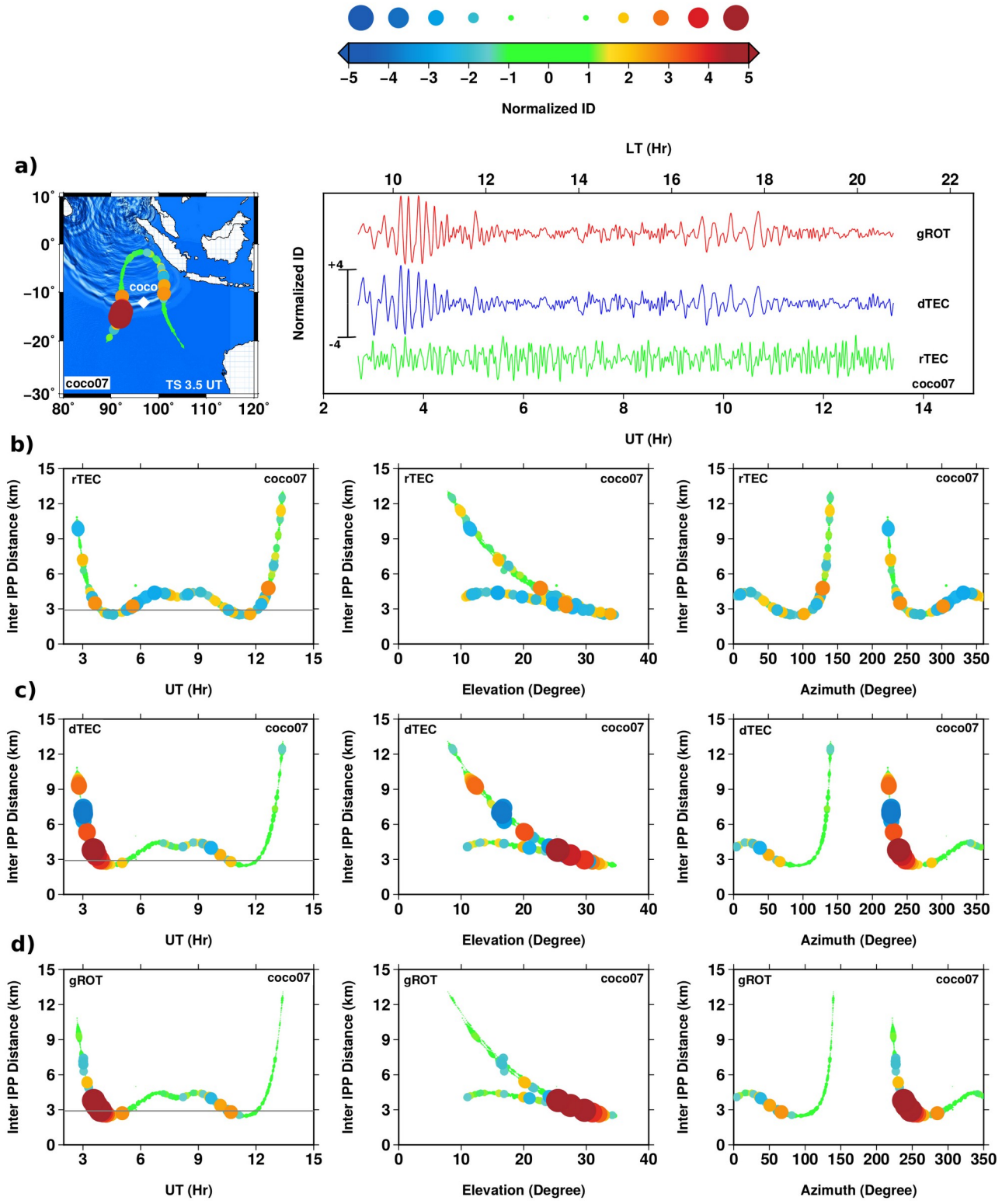

Figure 5: *(a) Spatiotemporal variation of TIP along the satellite track of COCO07 and simulated tsunami at 3.5 UT on 26th December 2004. Size and color of the circles on the satellite track represent amplitude of normalized gROT. White diamond is GPS station COCO. Time series of normalized gROT (red), dTEC(blue) and rTEC (green) for COCO07 are given in the right panel; (b), (c) and (d) Time-distance, elevation-distance and azimuth-distance plots color coded with normalized rTEC, dTEC and gROT of COCO07, respectively.*

TIP time series of COCO07 show that the amplitudes of TIPs in dTEC are higher than gROT up to 3.5 UT; but, rTEC did not detect any TIP (Fig. 5a). To explore the cause of difference in amplitudes, the TIPs are presented as a function of inter-IPP distance, elevation, and azimuth (Fig. 5b and 5c). It is evident from figures 5b and 5c that the difference between the amplitudes of dTEC and gROT increases with inter-IPP distance. Further, the difference also varies with both azimuth and elevation (Fig. 5b to 5d). The increase in the difference between amplitudes of TIPs, detected by the differential method and SPLA, with inter-IPP distance shows that the unaccounted inter-IPP distances are aliased as a signal in dTEC, particularly, at distances above 5 km which corresponds to elevation less than 25° and azimuth of ~225°.

As the elevation, azimuth and inter-IPP distance repeat in time and cause overlap when plotted as a function of time, we show the perturbations as a function of (i) time vs inter-IPP distance (time-distance plot) (Fig. 5b and 5c, left) and (ii) elevation vs distance (elevation-distance plot) (Fig. 5b and 5c, middle) and (iii) azimuth vs distance (azimuth-distance plot) (Fig. 5b and 5c, right). The time-distance plots of COCO07 color coded with normalized values of dTEC and gROT (Fig. 5c and 5d) distinguish the difference between TIP amplitudes obtained using the differential method and SPLA, particularly above 5 km of inter-IPP distance at 2-3 UT while the elevation angle was varying from 0°-20° (Fig. 5c and 5d). Similarly, the time-distance plots of COCO17 (Fig. 6) show that the signal aliasing occurs in dTEC at elevation below 15^{o} ($\Delta d > 8$km) is absent in gROT upon accounting the inter-IPP distance using SPLA. The differences in amplitude between dTEC and gROT exhibit that the amplitude aliasing in dTEC is caused by the unaccounted inter-IPP distances and show how possibly it could mislead the detection of ionospheric perturbations. Furthermore, the time-distance plots and elevation-distance plots (Fig. 6d) show that the aliases did not occur whenever the satellite is at low elevations, rather, the aliased signals are present only when the time and location of the TIPs coincide with the propagating tsunami (Fig. 6a). This further proves that the signal aliasing in dTEC is prominent only when the ionosphere is heterogeneous and

the aliasing increases with ionospheric heterogeneity. Hence, it is important to remove such aliasing by accounting the inter-IPP distance, particularly, while studying the ionospheric perturbations. On the other hand, the residual method completely failed to detect the signal in the case of COCO07, rather the rTEC time series is spurious during the entire span of the observation.

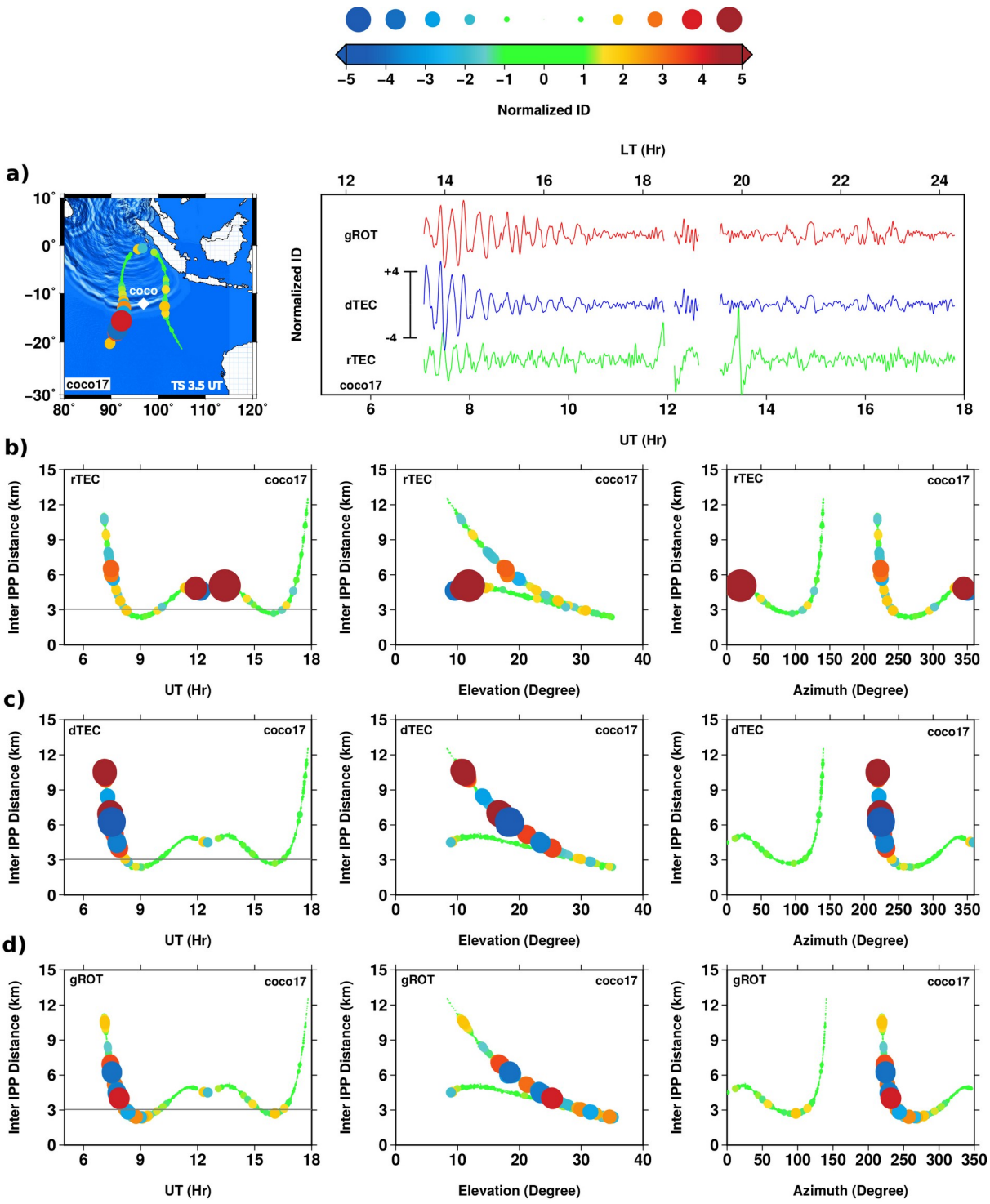

Figure 6: *Same as Figure 5 but for COCO17*

Apart from the observations made from the island GPS station COCO, we report two typical low elevation cases (IISC26 and HYDE29) observed from inland stations, which are not reported so far, to explain the significance of low elevation observation and critical inter-IPP distance (> 5 km) of strong aliasing (Fig. 7 and 8). The ionospheric perturbations coinciding with the tsunami propagating at 70^{o}E were observed by two GPS receivers located around 800 km away from the location of tsunami waves, that is IISC, Bangalore (13.0^{o} N, 77.5^{o}E) (Fig. 7a) and HYDE, Hyderabad (17.4^{o} N, 78.5^{o}E) (Fig. 8a), using signals transmitted by PRN26 and PRN29 respectively. The time series of IISC26 and HYDE29 and the time-distance plots show that the TIPs are detected by all the three methods. However, in the case of dTEC the presence of aliasing is prominent when the inter-IPP distance is above 5 km. Furthermore, there is a difference in phase as well as amplitude between rTEC and gROT. But, the difference is only in amplitude between dTEC and gROT (Fig. 7a). The cross correlation of rTEC and gROT (Table 1) reveals that the signal in rTEC is delayed by 330s in the case of HYDE29 and advanced by 180s in the case of IISC26. These two cases reveal that the TIPs observed by two different satellite-receiver pairs at low elevation angle cannot be due to multipath or any other error associated with the observational system or surrounding environment. The coincidence of location and time of TIPs with the simulated tsunami (Fig. 5, 6, 7 and 8), with a delay associated with time required for vertical propagation, further substantiates that the TIPs observed at low elevations are caused by the tsunami. Further, the elevation-distance and azimuth-distance plots (Fig. 7 and 8) show that the combination of low elevation and high azimuth keeps the inter-IPP distance less than 6 km. Hence, the aliasing in dTEC is less compared to COCO07 (Fig. 5) and COCO17 (Fig. 6) though the elevation of the observation is less than 20°. These results reveal that merely discarding the low elevation observation will not remove the aliasing, instead it will remove the possibility to detect the potential signals besides reducing the area of exploration. The above cases illustrate that accounting the inter-IPP distance, which is a function of both elevation and azimuth (Eq. 7), using SPLA while computing the

ionospheric perturbations will not only remove the amplitude of aliasing but also removes the necessity of excluding low-elevation observations. Eventually, SPLA helps to increase the area of ionospheric exploration by a single GPS receiver. Hence, SPLA can be a suitable candidate for tsunami early warning.

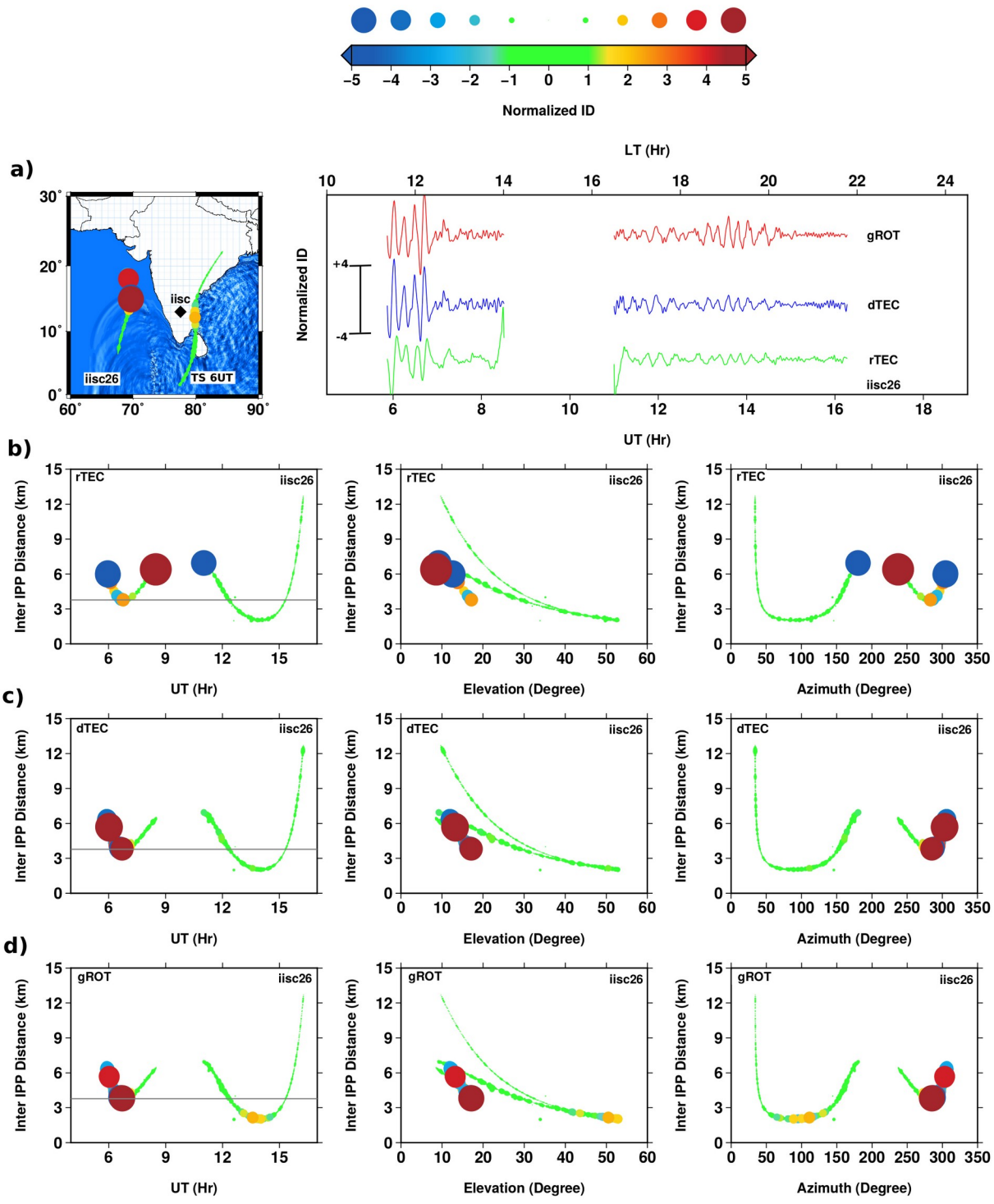

Figure 7: *Same as Figure 5 but for IISC26 and simulated tsunami is at 6UT*

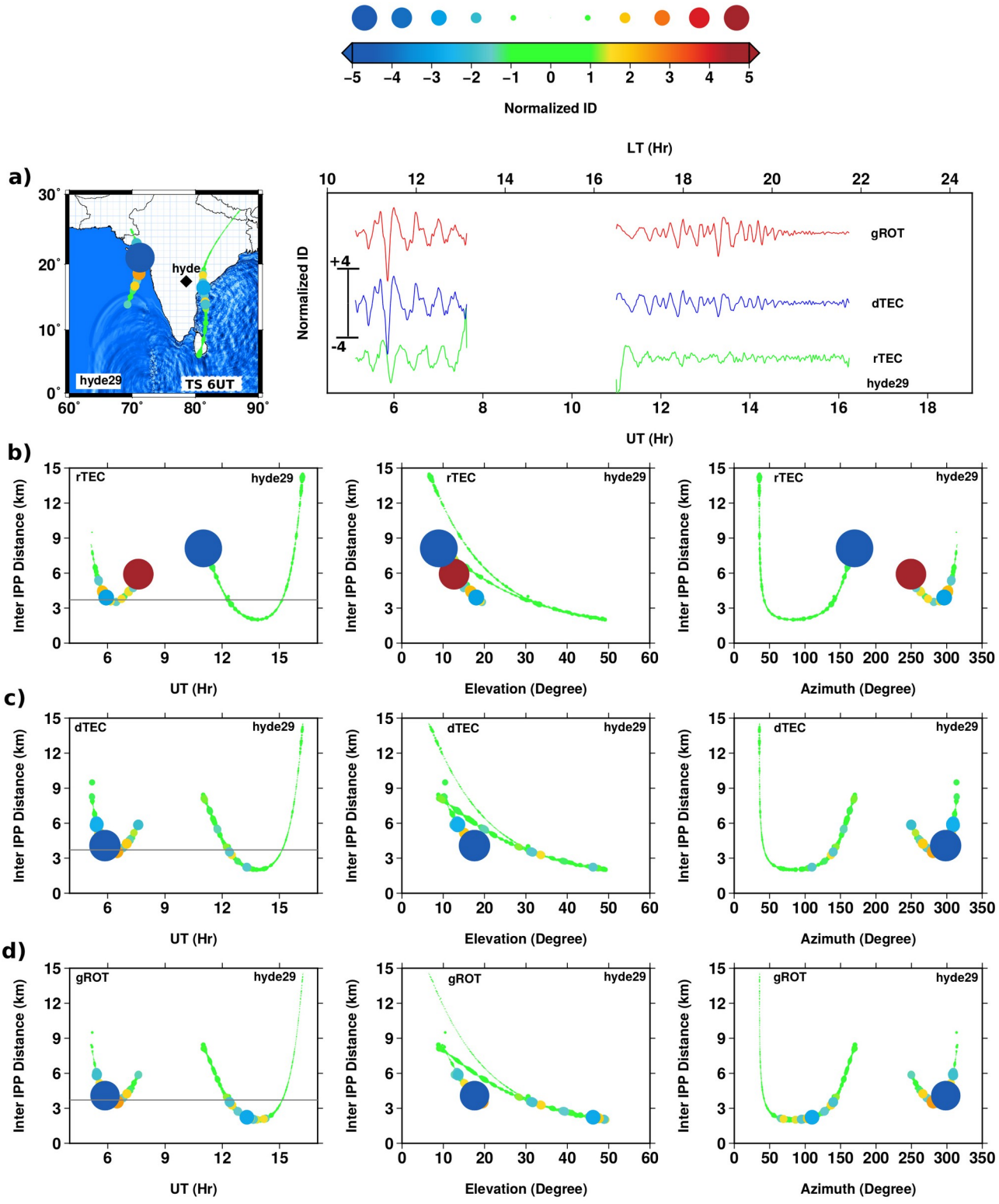

Figure 8: *Same as Figure 5 but for HYDE29 and simulated tsunami is at 6UT*

The time-distance plots of tsunami induced ionospheric perturbation presented in Fig. 9 show distinct aliases in dTEC at BAN231, COCO02, COCO04, DGAR07, and IISC11. The

perturbations derived using differential method (dTEC) contain signal aliases associated with inter-IPP distance in 27% of the detected cases (Table 1) when compared to gROT which is free of any such aliasing.

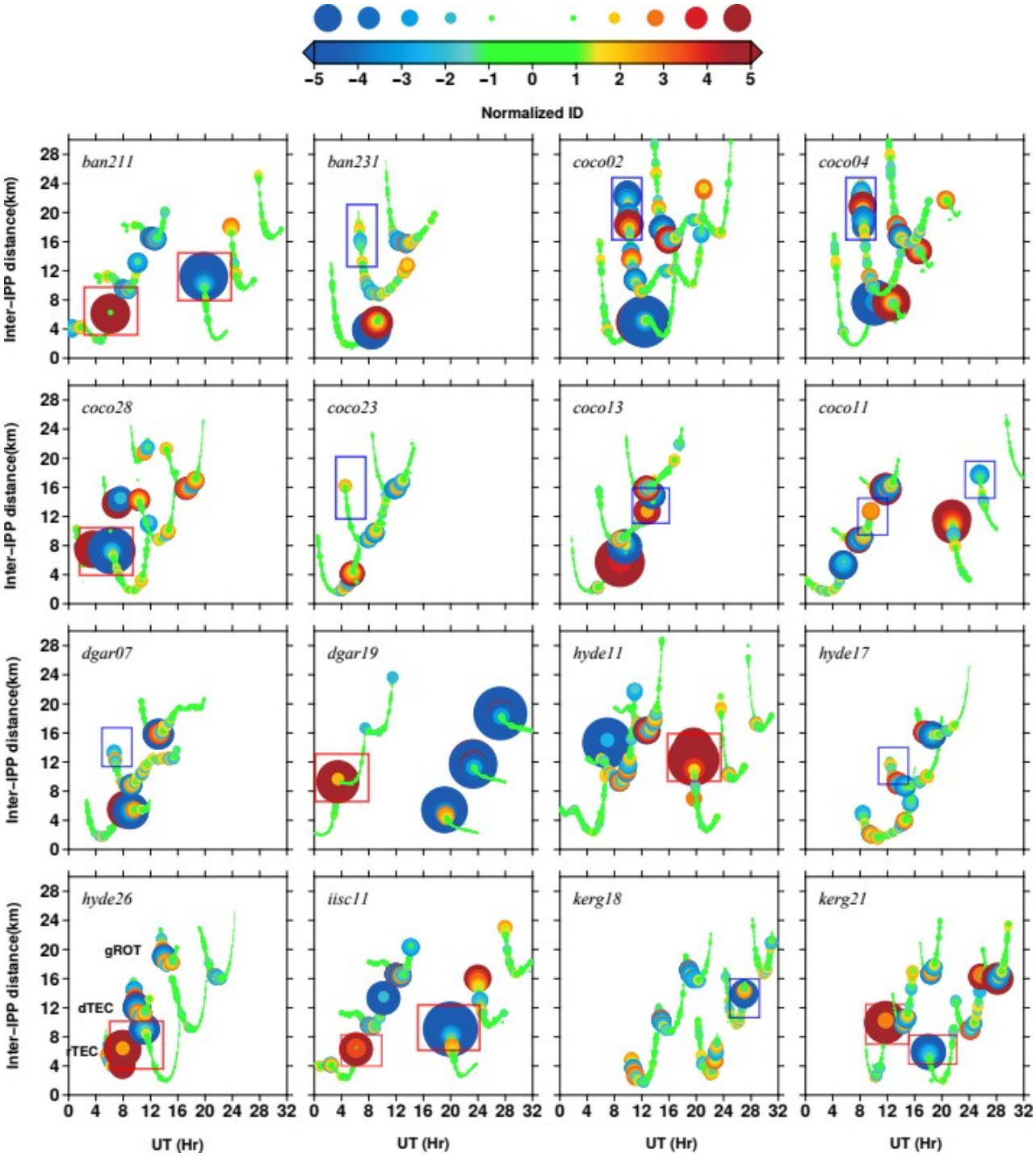

Figure 9: *TIPs induced by 26th December 2004 Indian ocean Tsunami derived using differential (dTEC), residual (rTEC) and SPLA (gROT) methods are plotted as a function of time vs. inter-IPP distance. Size and color of the circles represent amplitudes of the normalized TIPs. For better visual*

clarity dTEC is shifted in distance with 7km and 4hrs in time, gROT is shifted in distance with 14km and 8hrs in time. Red and blue boxes represent the artifacts and aliasing.

In contrast, the residual method has another shortcoming in the form of artifacts. The artifacts in rTEC arise due to the limitation in characterizing the trend of normal TEC variation, particularly, when the observation is discontinuous, for example, IISC26 (Fig. 7) and HYDE29 (Fig. 8). Similarly, multiple breaks between 11 and 14 UTC create a severe signal aliasing in rTEC of COCO17 (Fig. 6a) and such a strong signal is neither present in dTEC nor in gROT. Similar aliasing and artifacts in dTEC and rTEC at various satellite-PRN pairs are shown in Fig. 9.

6.5 Detecting aliasing and artifact free CIPs

Time-distance plots given in Fig. 10 show that the aliasing is prominent in CIPs obtained using the differential method (dTEC). There are significant differences in amplitude of gROT and dTEC in 61% of the cases when the inter-IPP distances are more than 4 km (Fig. 10), which indicate that unaccounted inter-IPP distances in differential method aliased as ionospheric perturbations in dTEC.

The scenario is completely different when using the residual method (rTEC). The rTEC values show strong signals in many cases at different times compared to dTEC and gROT (Fig. 10). Upon comparing these values with the corresponding time series (Fig. 11), one can easily identify that most of the signals are artifacts associated with data gaps. Other than artifacts, notable CIPs occur prior to the earthquake, for example, PYUT16 (Fig. 10). The corresponding time series given in Fig. 11 reveal that these are multiple artifacts occurred in a short time which caused this signal aliasing.

Apart from the artifacts and aliasing, time series of receiver-PRN pairs show that residual method (rTEC) completely failed to detect CIPs in 50% of the cases compared to the differential method and SPLA (Fig. 11 and Table 2). Upon exploring, we found that the poor fits of high order polynomials used to represent the trend of vTEC time series lead to failure in detecting the CIPs

(Fig. 12). For example, in the case of TPLJ03 (Fig. 12) it is shown that the polynomial fits well with vTEC only from 4 UT to 5:45 UT. However, the CIP detected by dTEC (Fig. 12c) and gROT (Fig. 12d) at 6:15 UT falls under the misfit region in the case of rTEC (Fig. 12b) which leads to failure in detecting the CIP by residual method. Further inspections revealed that the filtering process of obtaining CIPs from rTEC filtered out the high residual appear from 6:15 UT to 8:45 UT (Fig. 12b) and this lead to the failure of detecting the sharply varying CIP with a frequency range of 1.6 to 16 mHz by the residual method. However, such sharp variations were successfully detected by SPLA.

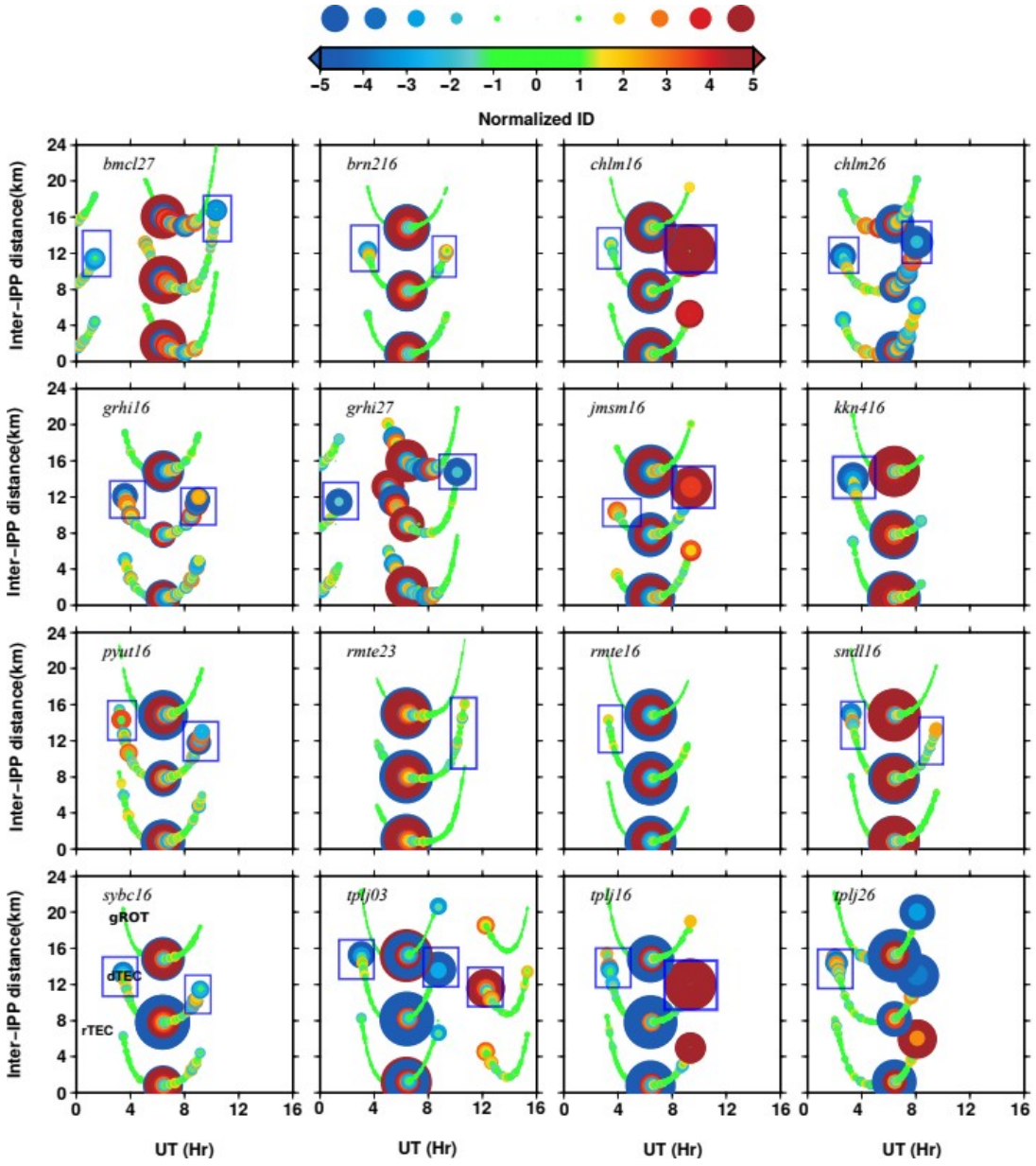

Figure 10: *CIPs induced by 25th April 2015 Nepal-Gorkha earthquake (occurred at 6:11:26 UT) derived using residual (rTEC), differential (dTEC) and SPLA (gROT) methods are plotted as a function of time vs. inter-IPP distance. Size and color of the circles represent the amplitudes of the normalized CIPs. For better clarity dTEC is shifted in distance with 7 km and gROT is shifted in distance with 14 km. Blue boxes represent aliasing.*

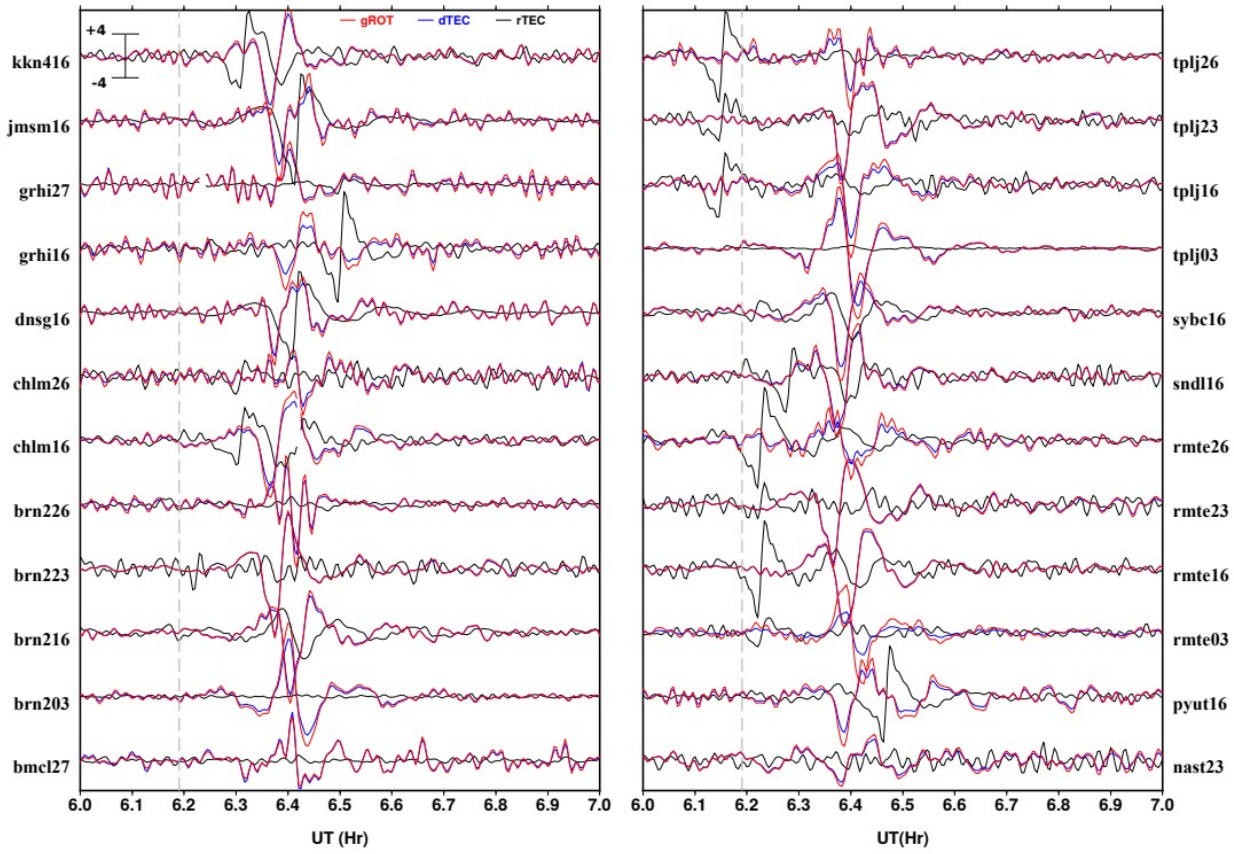

Figure 11: *Time series of CIPs: rTEC (black), dTEC (blue) and gROT (red) associated with the 2015 Nepal-Gorkha earthquake for selected satellite-receiver pairs (Local time for this case is UT+5:45). Grey dotted line represents time of the earthquake.*

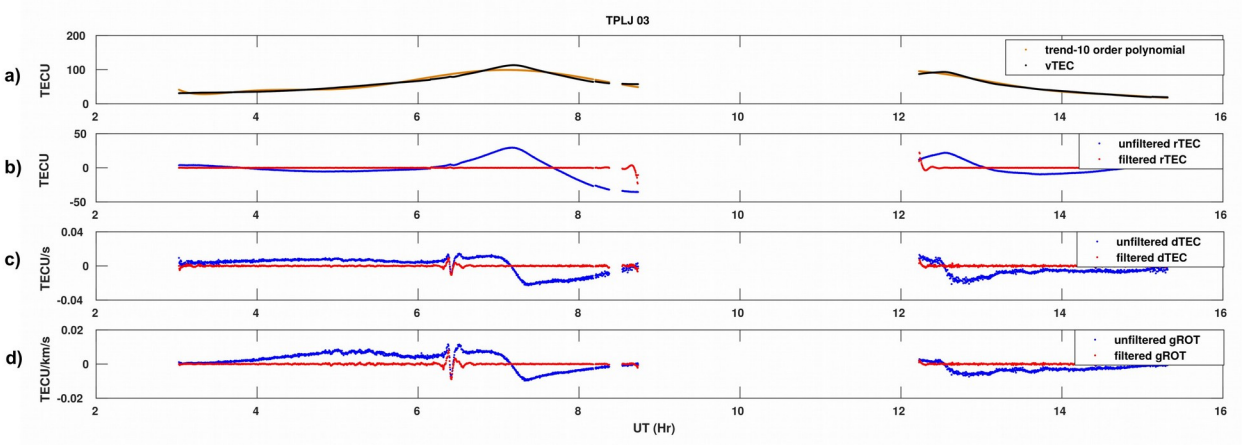

Figure 12: *(a) The process of obtaining CIP using residual method: the vertical TEC (vTEC) of TPLJ03 and the 10th order polynomial representing the trend. (b) residual rTEC and filtered rTEC (1.6 to 16.6 mHz), (c) unfiltered and filtered dTEC and (d) unfiltered and filtered gROT.*

6.6 Magnitude of aliasing

Ionospheric perturbations derived using residual method, differential method and SPLA from the GPS observations carried out during tsunami, and earthquake are presented as a function of inter-IPP distance (Fig. 13, left). As expected from the theoretical study carried out by Shimna and Vijayan (2020), in the real data set as well the rTEC and dTEC are invariant with inter-IPP distance and gROT varies as a function of distance (Fig. 13, left). Further, the values of gROT obtained in the two geophysical events are confined within the upper and lower theoretical bounds. The theoretical bounds were computed following Shimna and Vijayan (2020). These bounds are computed by considering a spatially homogeneous ionosphere, in which TEC varies at a constant rate (refer Fig. 1). The idea of computing the TB is to set a benchmark for exhibiting the impact of nonuniform spatial sampling (or inter-IPP distance) on ionospheric perturbation measurements. To obtain the TB, we considered a hypothetical ionosphere which is homogeneous in space; but varies at a constant rate (Fig. 1). Then, we computed spatiotemporal gradient of the hypothetical ionosphere measured using nonuniform spatial samples. If the spatiotemporal gradient of such an ionosphere is plotted as a function of inter-IPP distance, the spatiotemporal gradient measured along the track of uniform sampling will be a single value; but, the spatiotemporal gradient measured along the track of nonuniform spatial sampling will decrease gradually with distance (Fig. 1). Based on this idea, the upper (lower) theoretical bounds were computed assuming a constant rate of change of TEC which is equivalent to the maximum (minimum) value of ionospheric perturbation observed during the event. Assuming extreme possible perturbation values as a constant rate of change of TEC of a spatially homogeneous hypothetical ionosphere to compute the theoretical bounds (i.e. maximum perturbation for upper bound and minimum perturbation for lower bound)

will provide the least possible magnitude of aliasing present in the perturbations computed by different methods (refer Eq.12 and 13). In both tsunami and earthquake cases considered in this study, the highest perturbation values were obtained when adopting the residual method. Hence, to find the minimum possible level of aliasing which could present in the TIPs and CIPs, we selected the maximum and minimum perturbations obtained using the residual method to compute the theoretical bounds using the following equation.

$$TB_{upper} = \frac{IP_{max}}{\Delta d} \;\&\; TB_{lower} = \frac{IP_{min}}{\Delta d} \quad -(12)$$

where IP_{max} and IP_{min} are maximum and minimum ionospheric perturbations, respectively.

Separate theoretical bounds were computed for tsunami and earthquake cases using TIPs and CIPs computed using residual method.

The deviation of the ionospheric perturbations obtained using the three methods from the theoretical bound were quantified to understand the magnitude of aliasing

$$\delta_r = \left[\frac{|IP_n| - |T_B|}{|(T_B)|} \right]; \; |IP_n| - |TB| > 0 \quad -(13)$$

where δ_r is deviation relative to theoretical bound, IP_n is normalized ionospheric perturbation (dTEC or rTEC or gROT), and TB is theoretical bound.

The rTEC and dTEC deviate away from the theoretical bound with maximum relative deviations (δ_r) of 1.08 and 0.69, respectively (Fig. 13, left). However, the maximum deviation of gROT is only 0.33. It shows that SPLA is efficient in removing the impact of nonuniform spatial sampling.

Following Shimna and Vijayan (2020) and based on the confidence obtained from the experimental results (Fig. 13, left), average aliasing per kilometer of inter-IPP distance (A_l) in

rTEC, and dTEC are computed by considering gROT as the true value using the perturbations computed at all the IPP points during the two geophysical events.

$$A_l(\delta d) = \frac{\langle \| IP| - |gROT| \| \rangle_{\delta d}}{\langle |gROT| \rangle_{\delta d}} \quad -(14)$$

where A_l is average aliasing binned per km, *IP* is either rTEC or dTEC; δd is bin width. Average aliasing plotted as a function of inter-IPP distance (Fig. 13, right) reveals that the perturbations computed at uniform time interval (30 s for TIP and 15 s for CIP) with the implicit assumption of uniform spatial sampling (rTEC and dTEC) can amount to alter the magnitude of perturbations up to 2 times greater than the perturbations computed by accounting nonuniform spatial sampling interval (gROT). Further, the average aliasing of perturbations (Fig. 13, top right and bottom right) computed at 30 s sampling interval (TIP) and 15 s sampling interval (CIP) indicate that the magnitude of aliasing will not decrease with decreasing sampling rate as the difference between TEC values are proportional to the inter-IPP distances (refer Eq. 6) which, in turn, proportional to rate of sampling interval. For example, maximum inter-IPP distance in the case of CIP (15 s rate of sampling) is ~10 km (Fig. 13, bottom right) and of TIP (30 s rate of sampling) is ~18 km (Fig. 13, Top right). These results reveal the effectiveness of SPLA in detecting aliasing free TIPs and CIPs. Furthermore, these results signify the ease of computing ionospheric perturbations using SPLA from GPS observations carried out with heterogeneous rate of sampling without the need of any re-sampling.

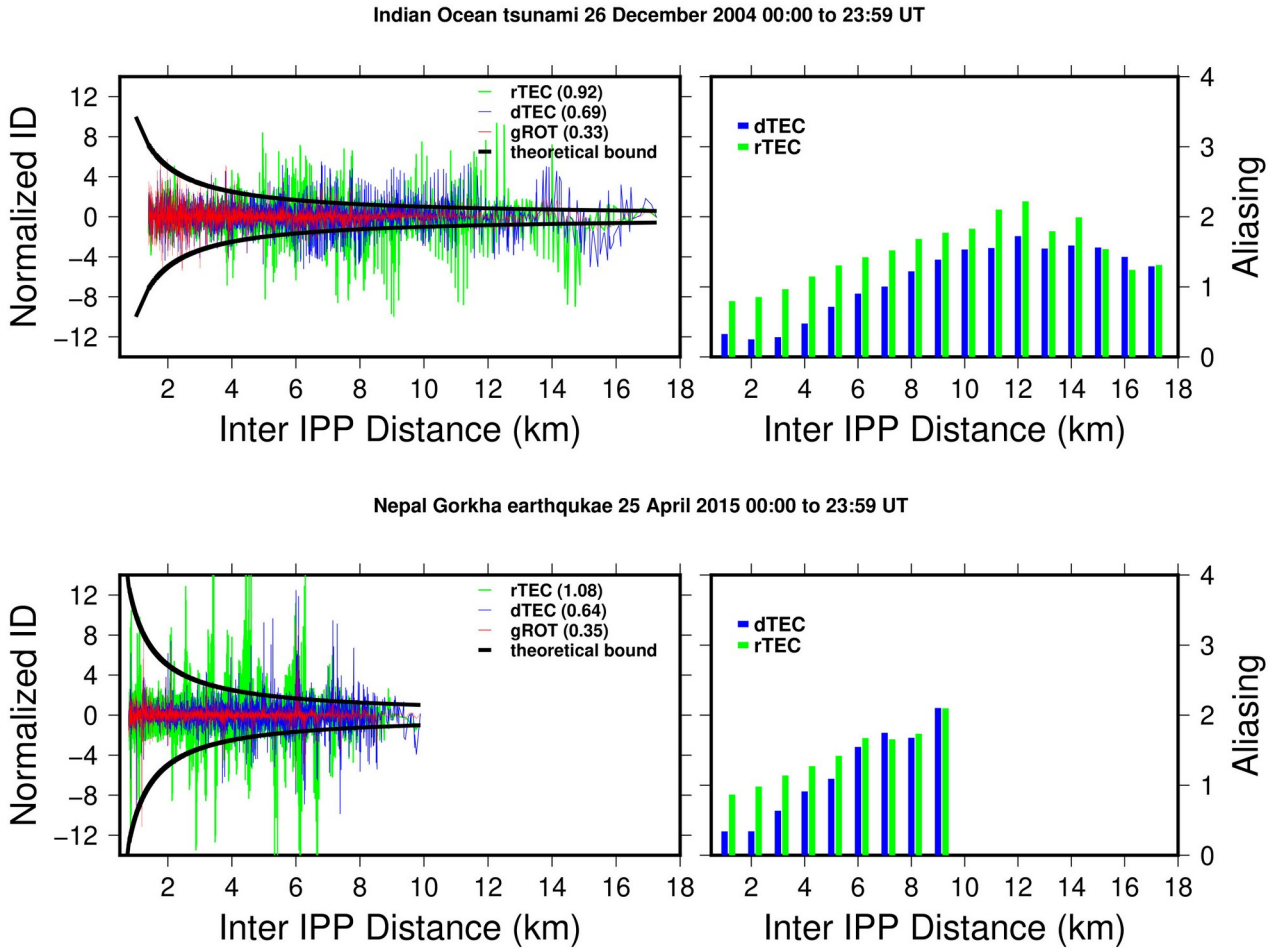

Figure 13: *(left) Variation of ionospheric perturbations with inter-IPP distances. (Right) Variation in magnitude of aliasing with inter-IPP distances.*

7 Impact of aliasing and artifact on characterization

The magnitude of aliasing indicated the impact of aliases due to the unaccounted inter-IPP distance on the amplitude of TIPs and CIPs. In this section, we further elaborate impacts of such unaddressed aliases and artifacts on phase, frequency, and Signal-to-Noise Ratio (SNR) of the ionospheric perturbations.

7.1 Impact on phase

Phase and time of occurrence of the ionospheric perturbations are the required parameters to determine velocity of the perturbations. The velocity of an ionospheric perturbation is one of the important characteristics as it directly affects the ray tracing which eventually leads to error in locating the source of the perturbation. To quantify the impact of aliases and artifacts on the phase,

we carried out a cross-correlation analysis and identified the difference in phase and time of occurrence between the perturbations obtained using the three methods. The gROT of each receiver-PRN pair was correlated with rTEC and dTEC, and the phase differences were converted into time differences. The results show that the occurrence time of TIP in rTEC is different from gROT. Among the 44 TIP time series, in 16 cases the time of occurrence of TIP in rTEC is delayed compared to gROT, in 17 cases rTEC detects TIPs prior to gROT and at 11 cases rTEC did not identify the TIPs (Table 1). The delay varies from 2.5 to 6.0 minutes and the advancement is ranging from 2.0 to 5.5 minutes (Fig. 14 and Table 1). The difference in time of occurrence between rTEC and gROT may be due to either aliasing or the subjective selection of the high-order polynomial to represent the trend of GPS TEC. Such differences in time of occurrence will consequently affect the characteristic velocity estimates of the tsunami induced ionospheric perturbations. However, there is no phase difference found between dTEC and gROT.

Similar to the tsunami case, the difference in time of occurrence between rTEC and gROT of CIPs are varying from 7.64 minutes of advancement to 2.55 minutes of delay (Fig.14,). Further, rTEC failed to detect 50% of CIPs (18 cases out of 36) compared to dTEC and gROT (Table 2). This difference in time of occurrence shows that the signal detection using residual method by employing uniform order of polynomial across all station-PRN pair mislead the detection. These results emphasize the importance of considering such methodology related differences while studying the physics of ionospheric perturbations.

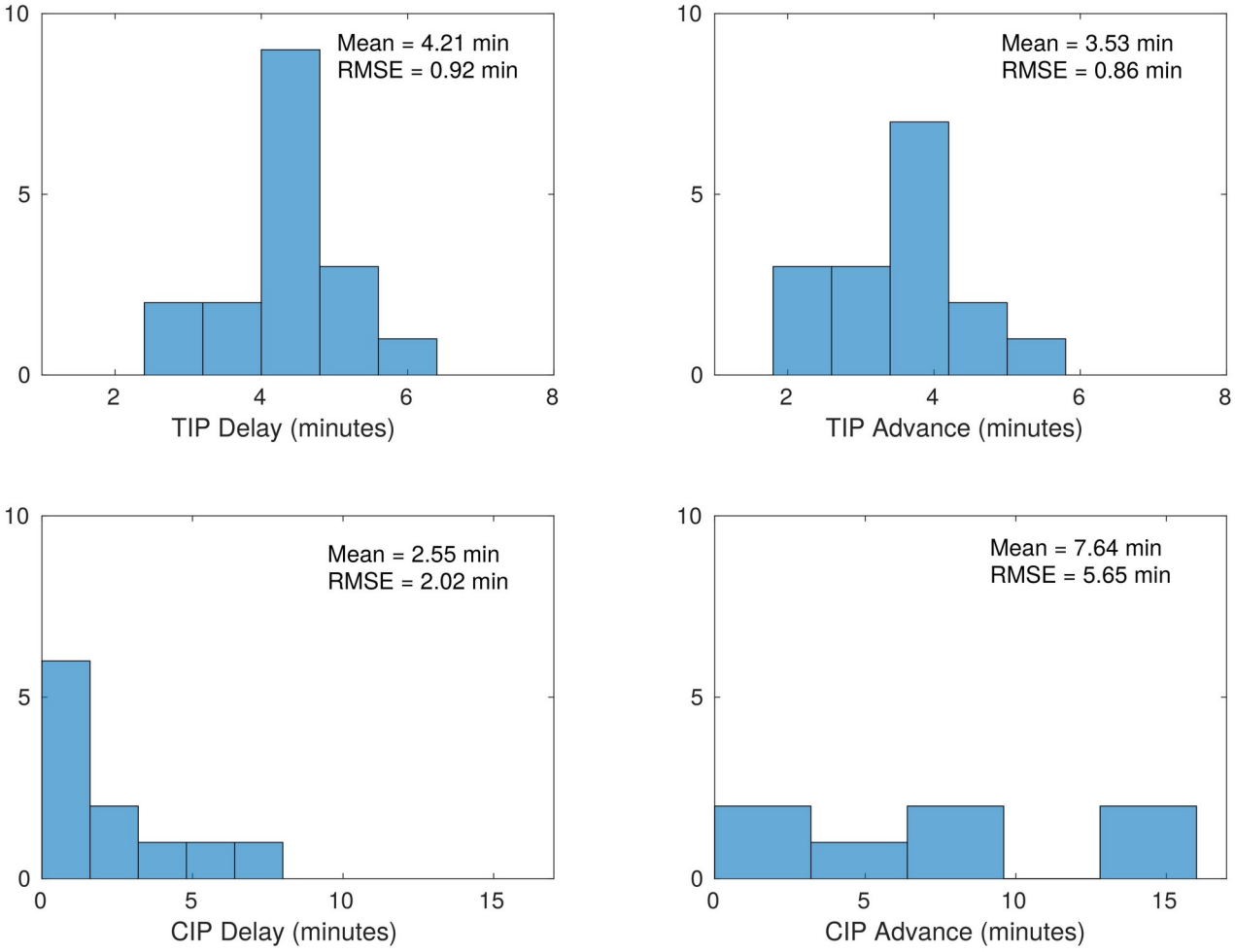

Figure 14: *Histogram of differences in time of occurrence between rTEC and gROT in TIPs and CIPs detected along each satellite track computed through cross correlation. Mean and RMS Error of the time differences (delays and advances) are given inside the respective figures.*

7.2 Impact on frequency

Frequency is one of the crucial parameters to differentiate the perturbations associated with different events. Hence, it is important to explore the frequencies of time varying inter-IPP distances along a satellite track. This will help to understand whether the band pass filter applied on ionospheric perturbation time series to filter the CIPs and TIPs also filters out the influence of inter-IPP distance or not. So, we transformed the time series of dTEC, inter-IPP distance, and gROT pertaining to two satellite tracks (DGAR04, and COCO23) from the time domain to frequency domain. The time series and their corresponding normalized Lomb-Scargle periodograms (Scargle, 1982) are given in Fig.15. The periodograms of inter-IPP distances (middle panel in Fig. 15) show that the frequencies of time varying inter-IPP distances are also lie within the frequency range

corresponding to the acoustic and acoustic-gravity components. Comparison of the periodograms of dTEC (left panel in Fig. 15), inter-IPP distance and gROT (right panel in Fig.15) indicates that the unaccounted inter-IPP distances got aliased as ionospheric perturbations in TIPs obtained using differential method (i.e. dTEC). Furthermore, the comparison reveals that the TIPs obtained using SPLA (i.e. gROT) is free of aliasing caused by inter-IPP distances. For example, the prominent portions (marked with green rectangles in Fig.15) of aliasing in dTEC and corresponding dealiased portions in gROT exhibit that SPLA not only removes the aliased signals; but also corrects the gain of the signals. Further, the periodograms shown in Fig. 15 indicate that the dealiasing by SPLA is effective throughout the spectra. The above results indicate that merely filtering the ionospheric perturbations using frequency filters without employing SPLA cannot filter out the aliases caused by unaccounted inter-IPP distances.

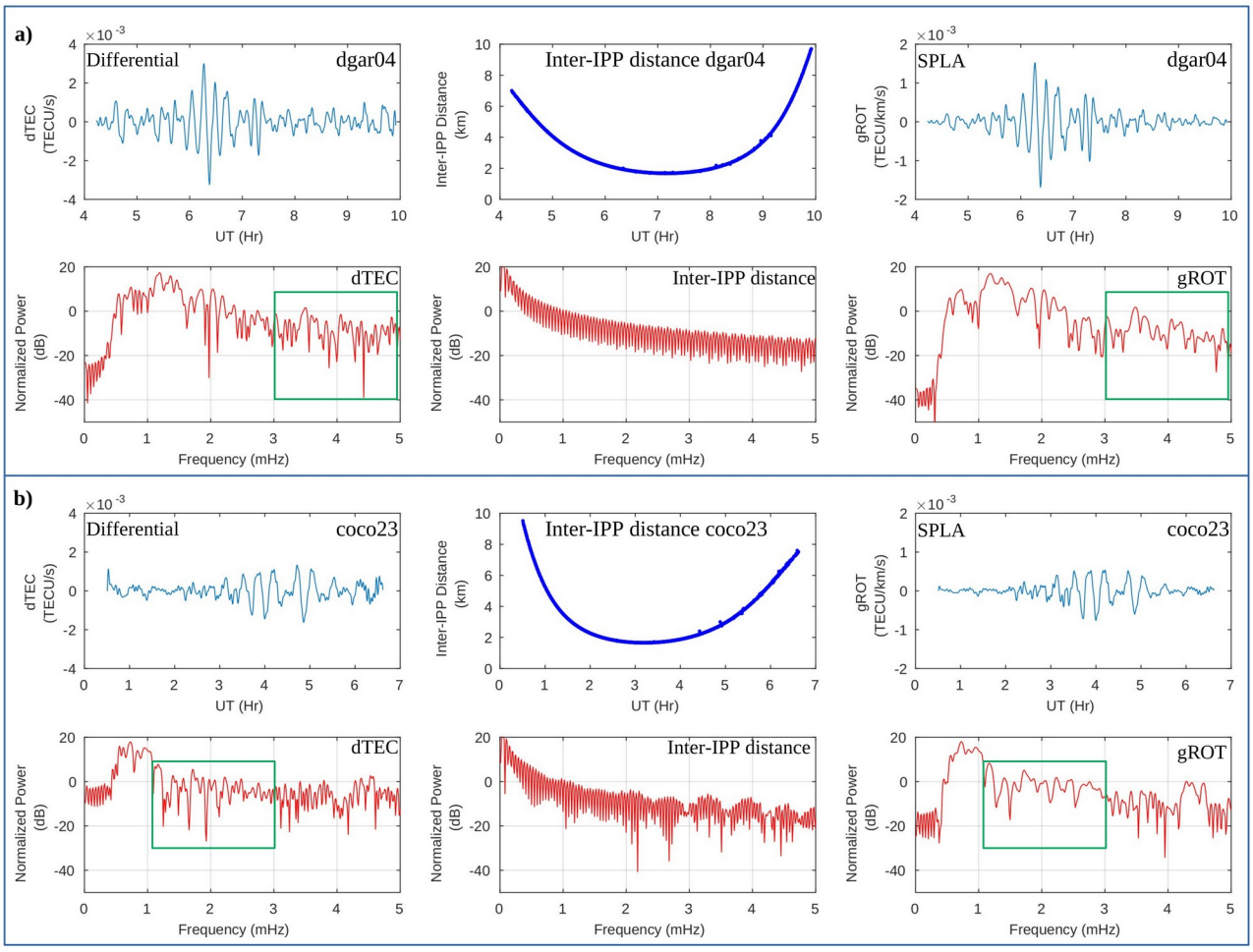

Figure 15: *Time series of TIP, inter-IPP distances, and its normalized Lomb-Scargle periodograms correspond to satellite-receiver pairs (a) dgar04 and (b) coco23. Top panels are time series of TIP obtained using differential method (left) and SPLA (right), and times series of inter-IPP distances (middle). Bottom panels are normalized Lomb-Scargle periodograms (red) of the respective time series (blue) given above. Frequencies of inter-IPP distances within the range of acoustic gravity component are only shown here for clarity. The prominent portion of aliased TIPs obtained by differential method (dTEC) and its dealiased counterpart obtained using SPLA (gROT) are marked with green boxes.*

We, further, tested differences in the frequency of perturbations obtained by adopting the differential, residual and SPLA methods using CWT analysis (Grinsted et al., 2004). Results reveal the significant variation in frequency between the residual method and SPLA. We present two typical cases here, in which one is similar to the second scenario demonstrated in the theoretical study (COCO17) and another one (COCO07) is a clear detection of TIP by gROT when the residual method finds the entire time series noisy (Fig. 16).

Time series of COCO17 show that in gROT and dTEC a strong TIP appears between 7 to 8 UT and a weak TIP appears between 11 to 14 UT along with two observational breaks. However, in rTEC, the weak TIP along with breaks (Fig. 6), similar to the second scenario in the theoretical study (Fig. 2), amplified greater than the strong TIP observed in gROT and dTEC between 7 to 8 UT. The corresponding CWT also shows that the artifacts in rTEC caused by the discontinuities in observation aliased as a strong signal within the frequency range of acoustic gravity wave induced TIPs. On the other hand, the frequencies of TIPs detected by gROT are clear and well confined within the expected range of 0.5 to 5 mHz (33 to 3.3 minutes). Furthermore, the CWT of gROT detects TIPs of small amplitude at 14 to 15 UT as shown in the theoretical case and distinctly detects the discontinuities in observations without any aliasing compared to dTEC.

In the case of COCO07, the residual method completely failed to detect the TIP which is present at the beginning of dTEC and gROT time series (Fig. 17). This is due to the misfit of 10^{th} order polynomial used to represent the trend of vTEC, particularly at the beginning and end of the observation (Fig. 17). This reveals the reason for the failure of the residual method to detect the perturbations occurring at the beginning and end of the observations. Further, the TIP time series of dTEC and gROT, and their corresponding CWTs show the difference between dTEC and gROT is due to the aliasing in dTEC (Fig. 16). This further emphasises the significance of removing the aliases and selection of appropriate method to detect the ionospheric perturbations. Furthermore, CWTs of these observations establish the resolving ability of SPLA and its capability of detecting ionospheric perturbations without aliasing under all conditions.

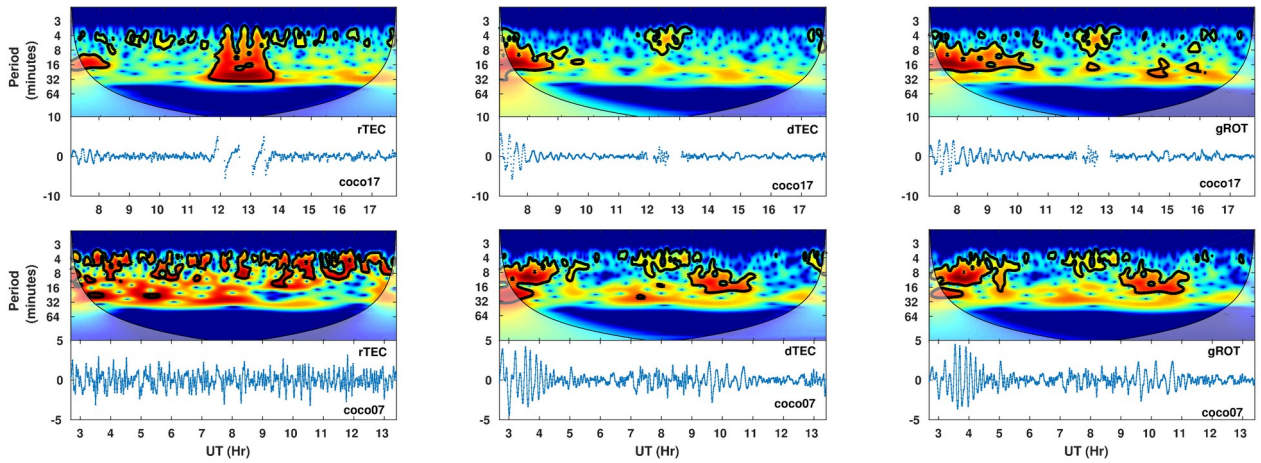

Figure 16: *Continuous Wavelet Transform of TIPs obtained along COCO17 and COCO07 using residual method, differential method and SPLA.*

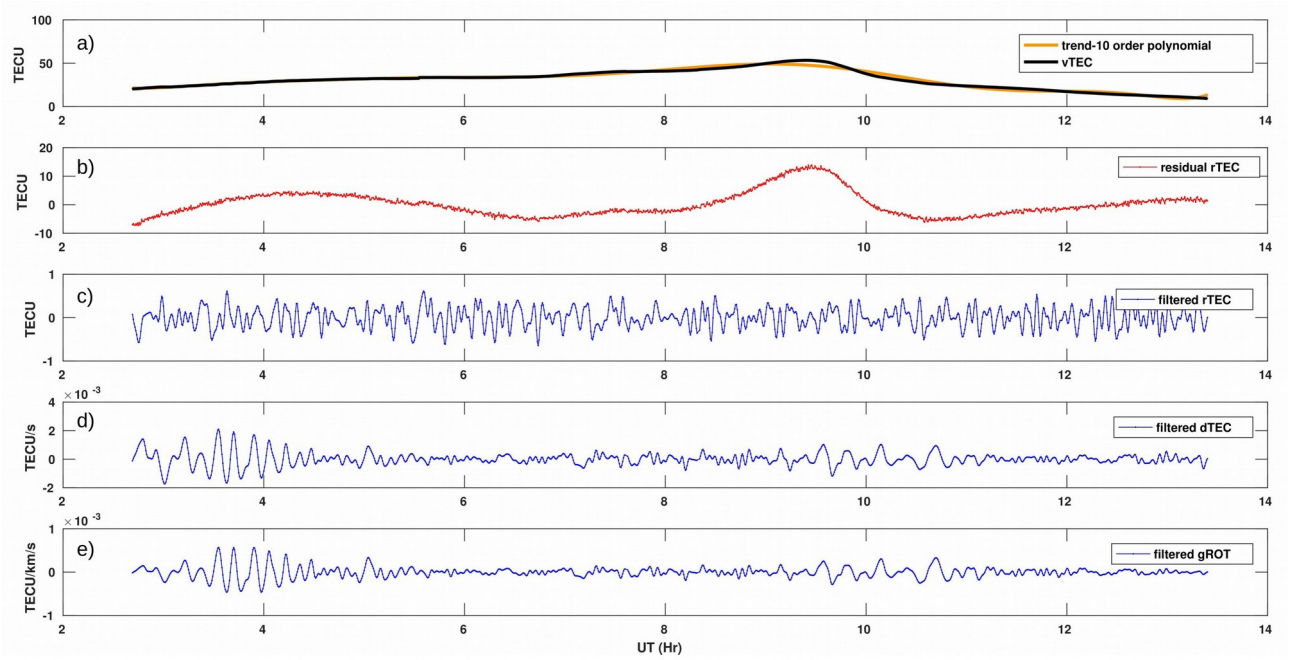

Figure 17: *(a) A 10th order polynomial trend fitted to the vTEC of COCO07. (b) Residual obtained from the trend fitted to the 10th order polynomial. (c) Filtered rTEC, (d) dTEC and (e) gROT computed using SPLA.*

7.3 Impact on Signal-to-Noise Ratio

Signal-to-Noise Ratio (SNR) of normalized TIPs and CIPs were computed for each aliasing and artifact free signal portion (δw) along the satellite tracks considering noise level as ±1.5 units in the normalized scale. The noise level was obtained from maximum peak-to-peak amplitude (range)

of the ionospheric perturbations computed along the satellite tracks on a quiet day (i.e. previous day of the tsunami and earthquake).

$$SNR = \left(\frac{IP_{max} - IP_{min}}{N} \right)_{\delta w} \quad -(15)$$

where *IP* is ionospheric perturbation (TIP or CIP), *N* is noise level.

Comparison of SNR of TIPs and CIPs derived using all the three methods (Fig. 18, Table 1 and Table 2) shows that the SNR is better for the perturbations derived using SPLA. The average SNR of aliasing and artifact free TIPs and CIPs obtained using SPLA is 2.6, whereas average SNR of the perturbations obtained by adopting residual and differential methods are 1.4 and 2.0, respectively (Fig. 18, Top). Further, it is evident from Fig. 18 (bottom) that the average increase in gain of the perturbations detected by SPLA compared to residual (rTEC) and differential (dTEC) methods are 149.1% and 38.6 %, respectively.

Similarly, the average SNR of all TIPs and CIPs (including those which suffer aliasing and artifacts) derived using SPLA is also higher than the TIPs derived using the differential and residual methods (Table 1 and Table 2). Further, the range of SNR variation (1.68) and standard deviation (0.43) of gROT manifest the consistency in obtaining TIPs using SPLA. However, among the three methods, the range of SNR and standard deviation are very high for rTEC (Table 2) which reveals that TIPs obtained using the residual method is highly inconsistent. Similarly, in the case of CIPs, strength of the signals detected by the residual method differs from corresponding ones detected by SPLA (Table 2). Results of the SNR comparisons reveal the magnitude of the impact of aliasing and artifacts on signal strength of the perturbations. Further, this analysis reveals the efficiency of SPLA on increasing the signal strength of the ionospheric perturbations detected using GPS apart from removing aliasing and artifacts.

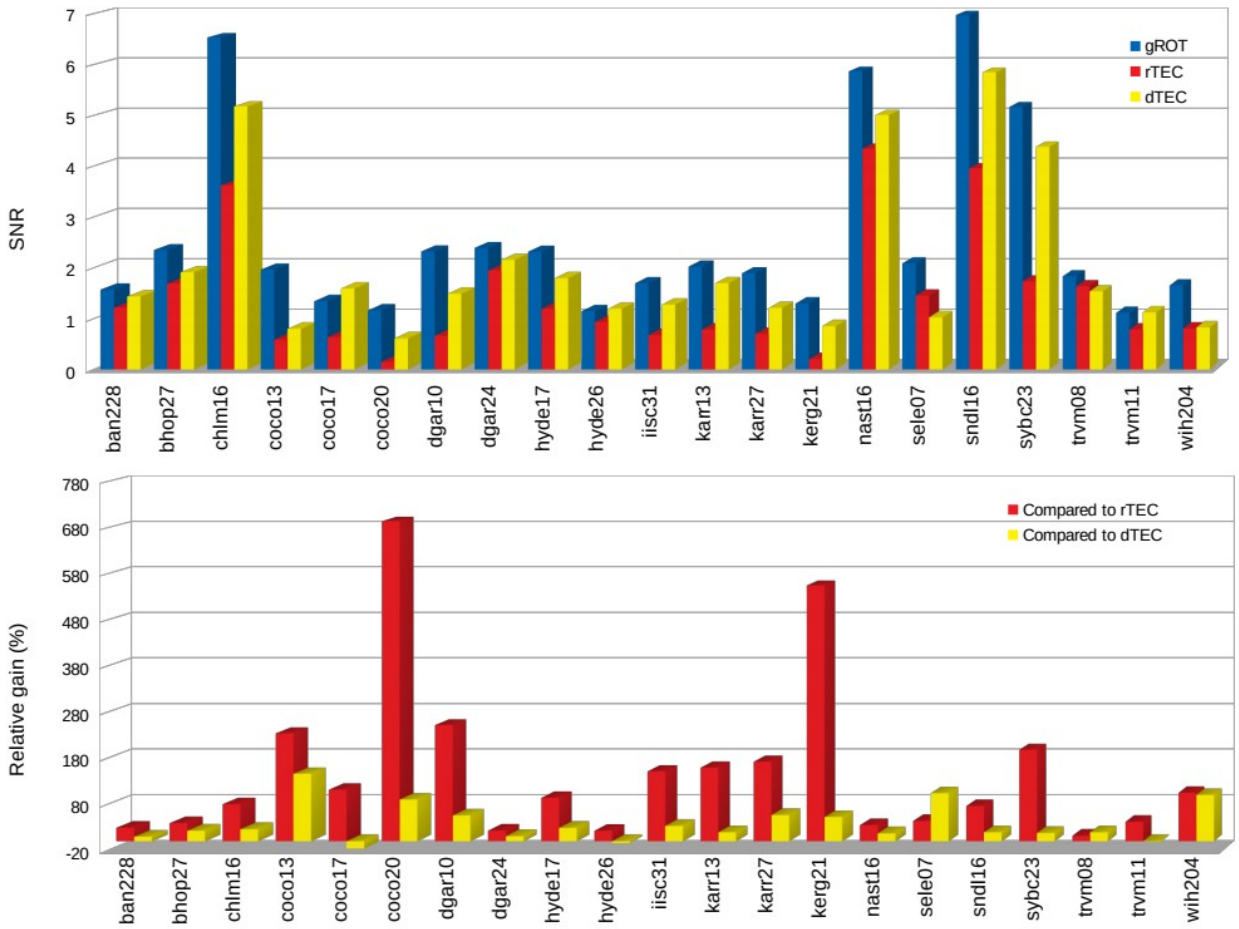

Figure 18: *(Top) Signal to Noise Ratio of gROT, rTEC and dTEC; (Bottom) Relative gain of gROT with respect to rTEC and dTEC*

Table 1: Signal-to-noise ratio (SNR) and difference in time of occurrence of TIPs computed using the three methods. Difference in time of occurrence was obtained by performing cross correlation of rTEC and dTEC time series with gROT.

TIP (Station-PRN)	SNR			Relative gain of gROT(%)		Remark	Time of occurrence compared to gROT(s)		Remark
	gROT	rTEC	dTEC	rTEC	dTEC		rTEC	dTEC	
ban211	1.62	-	1.26	-	27.89	Artifact	-	0.00	-
ban228	1.57	1.22	1.43	29.27	9.65		270.00	0.00	rTEC delayed with gROT
ban231	1.74	-	1.08	-	62.19		-	0.00	-
bhop27	2.35	1.69	1.91	39.01	22.87		-240.00	0.00	feeble rTEC
coco02	1.71	-	1.05	-	62.89	signal aliasing+artifact	-	0.00	-
coco04	1.68	-	0.73	-	131.03	signal aliasing	-	0.00	-
coco07	1.42	0.79	1.32	80.02	7.55	signal aliasing +artifact	-120.00	0.00	feeble rTEC
coco11	2.63	0.27	1.20	869.33	119.45	signal aliasing + artifact	240.00	0.00	feeble rTEC
coco13	1.96	0.59	0.80	234.05	146.18		300.00	0.00	rTEC delayed with gROT
coco17	1.34	0.63	1.59	111.75	-15.67		-180.00	0.00	feeble rTEC
coco20	1.16	0.15	0.61	693.93	90.35		-270.00	0.00	rTEC advanced with gROT
coco23	1.70	0.82	1.19	107.87	43.03	Artifact	330.00	0.00	feeble rTEC
coco24	1.67	0.21	0.89	680.45	86.44	signal aliasing	-180.00	0.00	rTEC advanced with gROT
coco28	1.65	-	0.58	-	185.94		-	0.00	-
coco31	1.87	0.76	1.40	144.09	32.99	Artifact	150.00	0.00	feeble rTEC
dgar07	2.16	-	1.04	-	108.44		-	0.00	-
dgar10	2.32	0.66	1.49	251.72	55.89		240.00	0.00	rTEC delayed with gROT
dgar17	1.78	-	1.21	-	46.51		-	0.00	-
dgar24	2.39	1.94	2.16	23.05	11.01		210.00	0.00	rTEC delayed with gROT
hyde08	2.30	1.24	1.32	85.70	74.50	signal aliasing + artifact	-330.00	0.00	rTEC advanced with gROT
hyde11	1.81	-	1.22	-	48.22		-	0.00	-
hyde17	2.32	1.19	1.80	94.22	29.00		-210.00	0.00	feeble rTEC
hyde19	1.19	-	0.53	-	124.11		-	0.00	-
hyde26	1.15	0.93	1.19	22.67	-3.85		360.00	0.00	rTEC delayed with gROT
hyde28	1.42	1.19	1.19	19.31	19.72	Artifact	-240.00	0.00	rTEC advanced with gROT
hyde29	1.43	1.12	1.42	27.11	0.12	Artifact	330.00	0.00	feeble rTEC
iisc11	1.66	-	1.26	-	32.12		-	0.00	-
iisc26	1.45	1.01	1.30	43.75	11.12	signal aliasing	-180.00	0.00	rTEC advanced with gROT
iisc28	1.29	1.15	1.18	12.62	9.22	Artifact	-270.00	0.00	rTEC advanced with gROT
iisc31	1.69	0.67	1.27	151.35	33.11		270.00	0.00	rTEC delayed with gROT
karr13	2.03	0.78	1.70	159.44	19.34		-210.00	0.00	rTEC advanced with gROT

karr23	1.31	1.10	1.35	18.63	-3.27	signal aliasing	-210.00	0.00	rTEC advanced with gROT
karr27	1.89	0.70	1.21	172.16	56.70		240.00	0.00	feeble rTEC
kerg21	1.30	0.20	0.85	554.81	52.40		240.00	0.00	feeble rTEC
kodi11	1.01	-	0.73	-	38.31		-	0.00	-
luma28	2.13	1.19	1.20	78.30	76.77	signal aliasing	270.00	0.00	rTEC delayed with gROT
pol207	2.20	0.73	0.86	202.36	157.02	Artifact	240.00	0.00	rTEC delayed with gROT
pol231	2.69	1.04	1.43	159.82	89.03	signal aliasing	240.00	0.00	rTEC delayed with gROT
sele07	2.09	1.45	1.02	43.91	103.97		-240.00	0.00	rTEC advanced with gROT
sele31	2.37	1.76	1.14	34.73	108.86	signal aliasing	-210.00	0.00	rTEC advanced with gROT
sey102	1.87	3.69	0.90	-49.21	108.98	signal aliasing	150.00	0.00	rTEC delayed with gROT
trvm08	1.83	1.64	1.53	12.00	19.41		-150.00	0.00	rTEC advanced with gROT
trvm11	1.11	0.78	1.12	41.93	-1.01		-150.00	0.00	rTEC advanced with gROT
wih204	1.65	0.81	0.83	105.19	100.22		210.00	0.00	rTEC delayed with gROT
Average SNR	1.77	1.03	1.19	159.25	57.70				
Maximum SNR	2.69	3.69	2.16	869.33	185.94				
Minimum SNR	1.01	0.15	0.53	-49.21	-15.67				
Standard deviation	0.43	0.65	0.34	218.87	49.24				
Range	1.68	3.54	1.62	918.54	201.61				

		Maximum delay	360.00
Percentage of TIPs not detected by the residual method	**25%**	**Minimum delay**	150.00
		Minimum advancement	-120.00
		Maximum advancement	-330.00

Table 2: Signal-to-noise ratio (SNR) and difference in time of occurrence of CIPs computed using the three methods. Difference in time of occurrence was obtained by performing cross correlation of rTEC and dTEC time series with gROT.

CIP (station-PRN)	SNR			Relative gain of gROT(%)		Remark	Time of occurrence compared to gROT (s)		Remark
	gROT	rTEC	dTEC	rTEC	dTEC		rTEC	dTEC	
bmcl27	4.278	-	4.708	-	-9.138	Signal aliasing +Artifact	-	0.000	-
brn203	7.570	-	5.879	-	28.768	Signal aliasing	-	0.000	-
brn216	6.902	3.084	6.091	123.784	13.313	Signal aliasing +Artifact	120.000	0.000	rTEC delayed with gROT
brn223	7.788	-	7.582	-	2.722		-	0.000	-
brn226	6.860	-	5.429	-	26.374	Signal aliasing	-	0.000	-
chlm16	6.533	3.621	5.177	80.393	26.185		-75.000	0.000	rTEC advanced with gROT
chlm26	3.993	-	3.085	-	29.432	Signal aliasing +Artifact	-	0.000	-
dnsg16	5.386	5.365	4.461	0.394	20.726	Signal aliasing +Artifact	90.000	0.000	rTEC delayed with gROT
grhi16	4.806	6.816	3.005	-29.491	59.919	Signal aliasing	300.000	0.000	rTEC delayed with gROT
grhi27	3.974	-	3.339	-	18.986	Signal aliasing +Artifact	-	0.000	-
jmsm16	6.609	6.800	4.795	-2.806	37.830	Signal aliasing	75.000	0.000	rTEC delayed with gROT
kkn416	6.714	4.748	5.582	41.392	20.282	A+Signal aliasing +shift	-240.000	0.000	rTEC advanced with gROT
kkn426	2.793	3.619	2.004	-22.827	39.345	Signal aliasing	30.000	0.000	rTEC delayed with gROT
lck327	5.316	-	5.610	-	-5.248	Artifact	-	0.000	-
lck427	5.510	-	5.867	-	-6.090		-	0.000	-
lhaz03	8.674	-	6.939	-	25.015		-	0.000	-
nast16	5.866	4.343	5.007	35.064	17.166		90.000	0.000	rTEC delayed with gROT
nast23	3.200	-	2.650	-	20.756		-	0.000	-
nast26	2.410	-	2.438	-	-1.154		-	0.000	-
npgj27	5.319	-	4.291	-	23.970		-	0.000	-
pyut16	5.406	5.888	3.899	-8.176	38.676	A+shift+Signal aliasing	210.000	0.000	rTEC delayed with gROT
rmte03	6.067	-	2.637	-	130.094	A+shift	-	0.000	-
rmte16	6.059	5.971	5.676	1.485	6.759	A+shift	-510.000	0.000	rTEC advanced with gROT
rmte23	6.548	2.209	6.220	196.481	5.280	Signal aliasing +Artifact	120.000	0.000	rTEC delayed with gROT

rmte26	4.393	6.194	2.634	-29.069	66.780	Signal aliasing +Artifact	-570.000	0.000	rTEC advanced with gROT
smkt27	6.566	-	5.152	-	27.442	Signal aliasing +Artifact	-	0.000	-
sndl16	6.970	3.955	5.847	76.239	19.218		90.000	0.000	rTEC delayed with gROT
sndl23	5.061	2.820	3.917	79.514	29.209	Signal aliasing	90.000	0.000	rTEC delayed with gROT
sndl26	3.772	3.267	3.575	15.471	5.516	Signal aliasing	-15.000	0.000	rTEC advanced with gROT
sybc03	4.706	-	2.878	-	63.509		-	0.000	-
sybc16	6.573	2.869	5.227	129.138	25.762	Artifact	-	0.000	rTEC delayed with gROT
sybc23	5.165	1.732	4.379	198.279	17.946		465.000	0.000	rTEC delayed with gROT
tplj03	8.095	-	6.628	-	22.137	Signal aliasing	-	0.000	-
tplj16	6.399	3.914	4.646	63.501	37.742	Signal aliasing	-960.000	0.000	rTEC advanced with gROT
tplj23	6.339	2.939	5.848	115.639	8.387	Artifact	-	0.000	rTEC advanced with gROT
tplj26	5.060	5.561	3.337	-8.995	51.653	Signal aliasing +Artifact	-840.000	0.000	rTEC advanced with gROT
Average SNR	5.658	4.286	4.623	52.770	26.257				
Maximum SNR	8.674	6.816	7.582	198.279	130.094				
Minimum SNR	2.410	1.732	2.004	-29.491	-9.138				
Standard deviation	1.464	1.542	1.423	71.009	25.588				
Range	6.265	5.085	5.577	227.770	139.232		**Minimum delay**	30.000	
							Maximum delay	465	
Percentage of CIPs not detected by the residual method		**50%**					**Maximum advancement**	-960	
							Minimum advancement	-15.000	

8. Summary and Conclusion

Ionospheric perturbations induced by tsunamis and earthquakes are obtained from GPS-TEC sampled at uniform time intervals along the satellite tracks. However, such samplings are nonuniform in space. Not accounting such nonuniform spatial sampling while computing the ionospheric perturbations introduces signal aliasing, predominantly in the amplitude. All the methods hitherto used to detect the co-seismic and tsunamigenic ionospheric perturbations did not account the nonuniform spatial sampling while computing the perturbations. Further, the residual method, used as an alternative to differential method, introduces artifacts as selection of the order of polynomials in this method is subjective. Recently, Shimna and Vijayan (2020) proposed an algorithm called Spatio-Periodic Leveling Algorithm (SPLA) to remove such aliasing from ionospheric irregularities induced by geomagnetic storms.

In this study, we showed that adopting SPLA to compute tsunami and earthquake induced ionospheric perturbations are efficient in removing aliasing and artifacts.

We validated the efficiency of SPLA in removing aliasing and artifacts by performing efficiency tests. We performed efficiency tests, first, under two simulated scenarios and then using GPS observations carried out during the 26th December 2004 Indian Ocean tsunami, and the 25th April 2015 Nepal-Gorkha earthquake. Results of the efficiency tests reveal that SPLA is efficient in resolving the perturbations from sharp static variations. Further, the observational validation (Fig. 13) shows that the perturbations obtained using SPLA are within the expected values, whereas, dTEC (differential method) and rTEC (residual method) show clear deviation. The maximum deviation (δr) of rTEC and dTEC in the observational data set are 1.08 and 0.69 (Fig. 13). The validation furhter reveals that the uncorrected inter-IPP distances cause the magnitude of aliasing up to 2 units (Fig. 13). This emphasizes the importance of correcting the influence of inter-IPP distance while computing the ionospheric perturbations.

Analysis of perturbations obtained using the three methods show that uncorrected aliasing and artifacts severely impact the characteristics of ionospheric perturbations. An assessment of the impact of aliasing and artifacts showed that SNR of the aliasing and artifact free ionospheric perturbations computed using SPLA is ~39% and ~149% higher compared to the perturbations obtained using differential and residual methods, respectively (Fig. 18). Wavelet and cross-correlation analyses carried out on TIPs and CIPs reveal that the time of occurrence and frequency of the perturbations differ significantly between SPLA and residual methods (Fig. 14 and Fig. 16). Besides, the residual method fails to detect 25% of TIPs and 50% of CIPs which were detected by both differential method and SPLA (Tables 1 and Table 2). Further explorations showed that misfits of uniform high-order polynomial representing the trend of GPS-TEC caused the failure in the detection of the perturbations in the case of residual method (Fig. 12 and 17). Above all, the results shown in section 6.4 reveals that SPLA is a suitable candidate to obtain ionospheric perturbations at low elevation angles and employing SPLA will increase the area of ionospheric exploration by a GPS receiver.

Overall, this study shows that the residual method performs poorly compare to other methods in resolving sharp static variations from signals and misses to detect ionospheric perturbations. Hence, caution needs to be exercised while adopting residual methods in real-time detection for earthquake or tsunami early warning, particularly, the one like VARION – Variometric Approach for Real-Time Ionosphere Observation (Savastano et al., 2017) which uses both differential and residual approaches to obtain TIPs in real-time.

Despite the advantages, the perturbations obtained using SPLA bound to vary with the selection of ionospheric shell height (h_{max}). Hence, a careful selection of appropriate ionospheric shell height specific to the region and time of the ionospheric monitoring is essential while adopting SPLA to obtain ionospheric perturbations using GPS or any other Global Navigational Satellite Systems.

Acknowledgment:

Authors acknowledge the GPS data provided by International GNSS Network (IGS) (ftp://cddis.gsfc.nasa.gov), and UNAVCO (ftp://data-out.unavco.org/), CORS (https://geodesy.noaa.gov/CORS/). We thank IGS and CODE for providing GPS products. We also thank Cornell University for sharing COMCOT. KS acknowledges the financial support of CSIR for SRF fellowship (No.31/66(001)/2017-EMR-I dt:28/03/17) and AcSIR for their support. Both the authors profoundly thank the insightful reviews of the two anonymous reviewers and acknowledge their valuable comments which helped to improve the paper significantly. We sincerely thank Dr. Kavirajan Rajendran, Group Head and Co-ordinator, Multi-Scale Modelling Programme (MSMP), CSIR-4PI for all the support and encouragement.

References

Artru, J., Ducic, V., Kanamori, H., Lognonné, P., Murakami, M., 2005. Ionospheric detection of gravity waves induced by tsunamis. Geophysical Journal International, 160(3), 840-848.

Astafyeva, E., Heki, K., 2009. Dependence of waveform of near-field coseismic ionospheric disturbances on focal mechanisms. Earth, Planets and Space, 61(7), 939–943. https://doi.org/10.1186/BF03353206

Astafyeva, E., Zakharenkova, I., & Förster, M. 2015. Ionospheric response to the 2015 St. Patrick's Day storm: A global multi-instrumental overview. *Journal of Geophysical Research: Space Physics*, *120*(10), 9023-9037

Astafyeva, E., 2019. Ionospheric Detection of Natural Hazards. *Reviews of Geophysics*, *57*(4), 1265-1288.

Astafyeva, E., & Shults, K. 2019. Ionospheric GNSS Imagery of Seismic Source: Possibilities, Difficulties, and Challenges. Journal of Geophysical Research: Space Physics, 124(1), 534–543. https://doi.org/10.1029/2018JA026107

Azeem, I., Barlage, M., 2018. Atmosphere-ionosphere coupling from convectively generated gravity waves. Advances in Space Research, 61(7), 1931-1941.

Bagiya, M. S., Sunil, A. S., Sunil, P. S., Sreejith, K. M., Rolland, L., & Ramesh, D. S. 2017. Efficiency ofcoseismic ionospheric perturbations in identifying crustal deformation pattern: Case study based on Mw7.3 May Nepal 2015 earthquake. Journal ofGeophysical Research: Space Physics, 122, 6849–6857. https://doi.org/10.1002/2017JA024050

Bilitza, D., Altadill, D., Zhang, Y., Mertens, C., Truhlik, V., Richards, P., Reinisch, B., 2014. The International Reference Ionosphere 2012–a model of international collaboration. Journal of Space Weather and Space Climate, 4, A07.

Bock, Y., Melgar, D., & Crowell, B. W. 2011. Real-time strong-motion broadband displacements from collocated GPS and accelerometers. *Bulletin of the Seismological Society of America*, *101*(6), 2904-2925.

Catherine, J. K., Vijayan, M. S. M., Rabiya, U. S., Shimna, K., Gahalaut, V. K., Ramesh, D. S., 2015. Dichotomy in mode propagation of coseismic ionospheric disturbance: Observations from 11 April 2012 Indian Ocean earthquake. Journal of Geophysical Research: Space Physics, 120(5), 3854-3867.

Cherniak, I., Zakharenkova, I., & Redmon, R. J. 2015. Dynamics of the high-latitude ionospheric irregularities during the 17 March 2015 St. Patrick's Day storm: Ground-based GPS measurements. *Space Weather, 13(9),* 585-597.

Ducic, V., Artru, J., Lognonné, P., 2003. Ionospheric remote sensing of the Denali Earthquake Rayleigh surface waves. Geophysical Research Letters, 30(18).

Fan, W., & Shearer, P. M., 2015. Detailed rupture imaging of the 25 April 2015 Nepal earthquake using teleseismic P waves. Geophysical Research Letters, 42(14), 5744-5752.

Galvan, D. A., Komjathy, A., Hickey, M. P., Mannucci, A. J., 2011. The 2009 Samoa and 2010 Chile tsunamis as observed in the ionosphere using GPS total electron content. Journal of Geophysical Research: Space Physics, 116(A6).

Grinsted, A., Moore, J. C., Jevrejeva, S., 2004. Application of the cross wavelet transform and wavelet coherence to geophysical time series. Nonlinear processes in geophysics, 11(5/6), 561-566.

Havskov, J., & Alguacil, G. 2004. *Instrumentation in earthquake seismology* (Vol. 358). Dordrecht, The Netherlands: Springer.

Hebert, H., Sladen, A., Schindele, F., 2007. Numerical modeling of the great 2004 Indian Ocean tsunami: focus on the Mascarene Islands. Bulletin of the Seismological Society of America, 97(1A), S208-S222.

Hickey, M. P., Schubert, G., Walterscheid, R. L., 2009. Propagation of tsunami driven gravity waves into the thermosphere and ionosphere. Journal of Geophysical Research: Space Physics, 114(A8).

Hoffmann, L., Wu, X., Alexander, M. J., 2018. Satellite observations of stratospheric gravity waves associated with the intensification of tropical cyclones. Geophysical Research Letters, 45(3), 1692-1700.

Jakowski, N., Hoque, M. M., 2019. Estimation of spatial gradients and temporal variations of the total electron content using ground based GNSS measurements. Space Weather, 17(2), 339-356.

Jin, S., Occhipinti, G., Jin, R. 2015. GNSS ionospheric seismology: Recent observation evidences and characteristics. Earth-Science Reviews, 147, 54–64. https://doi.org/10.1016/j.earscirev.2015.05.003

Klobuchar, J.,1987. Ionospheric Time-Delay Algorithm for Single-Frequency GPS Users. IEEE Transactions on Aerospace and Electronic Systems, AES-23(3), 325–331. https://doi.org/10.1109/TAES.1987.310829

Komjathy, A., Yang, Y. M., Meng, X., Verkhoglyadova, O., Mannucci, A. J., Langley, R. B., 2016. Review and perspectives: Understanding natural hazards generated ionospheric perturbations using GPS measurements and coupled modeling. Radio Science, 51(7), 951-961.

Kong, J., Yao, Y., Zhou, C., Liu, Y., Zhai, C., Wang, Z., Liu, L., 2018. Tridimensional reconstruction of the Co-Seismic Ionospheric Disturbance around the time of 2015 Nepal earthquake. Journal of Geodesy, 92(11), 1255-1266.

Lay, T., Kanamori, H., Ammon, C. J., Nettles, M., Ward, S. N., Aster, R. C., DeShon, H. R., 2005. The great Sumatra-Andaman earthquake of 26 december 2004. Science, 308(5725), 1127-1133.

Liu, J. Y., Lin, C. H., Tsai, H. F., & Liou, Y. A. 2004. Ionospheric solar flare effects monitored by the ground-based GPS receivers: Theory and observation. *Journal of Geophysical Research: Space Physics*, *109*(A1). Check again

Liu, J. Y., Tsai, Y. B., Ma, K. F., Chen, Y. I., Tsai, H. F., Lin, C. H., . Lee, C. P., 2006. Ionospheric GPS total electron content (TEC) disturbances triggered by the 26 December 2004 Indian Ocean tsunami. Journal of Geophysical Research: Space Physics, 111(A5).

Liu, P. L., Woo, S. B., Cho, Y. S., 1998. Computer programs for tsunami propagation and inundation. Technical Report, Cornell University, *25*.

Manta, F., Occhipinti, G., Feng, L., & Hill, E. M. 2020. Rapid identification of tsunamigenic earthquakes using GNSS ionospheric sounding. Scientific Reports, 10(1), 11054. https://doi.org/10.1038/s41598-020-68097-w

Occhipinti, G. 2015 Chap. 9: The Seismology of Planet Mongo, the 2015 Ionospheric Seismology Review, AGU Books, G*eodynamics*, eds Morra, G., Yuen, D., Lee, S. & King, S., ISBN: 978-1-118-88885-8. doi: 10.1002/9781118888865.ch9

Occhipinti, G., Rolland, L., Lognonné, P., & Watada, S. 2013. From Sumatra 2004 to Tohoku-Oki 2011: The systematic GPS detection of the ionospheric signature induced by tsunamigenic earthquakes. Journal of Geophysical Research: Space Physics, 118(6), 3626–3636. https://doi.org/10.1002/jgra.50322

Prikryl P., Ghoddousi-Fard R., Kunduri BSR., Thomas EG., Coster AJ., Jayachandran PT., Spanswick E., & Danskin DW. 2013. GPS phase scintillation and proxy index at high latitudes during a moderate geomagnetic storm. *Annales of Geophysicae 31*, 805–816. https://doi.org/10.5194/angeo-31-805-2013

Rao, P. R., Niranjan, K., Prasad, D. S. V. V. D., Krishna, S. G., Uma, G., 2006. On the validity of the ionospheric pierce point (IPP) altitude of 350 km in the Indian equatorial and low-latitude sector. In Annales Geophysicae, 24(8), 2159-2168).

Rolland, L. M., Lognonné, P., & Munekane, H., 2011. Detection and modeling of Rayleigh wave induced patterns in the ionosphere. Journal of Geophysical Research: Space Physics, 116(A5). https://doi.org/10.1029/2010JA016060

Scargle, J. D. 1982. Studies in astronomical time series analysis. II-Statistical aspects of spectral analysis of unevenly spaced data. *The Astrophysical Journal*, *263*, 835-853

Shimna,K., Vijayan,M.S.M. ,2018. A simple algorithm to remove artefacts and aliasing from the ionospheric irregularities detected using GPS, C1.4, 42nd COSPAR Scientific Assembly 2018, 14-22 July 2018, Pasadena, CA,US.

Shimna, K., Vijayan, M. S. M. 2020. Detecting ionospheric disturbances using GPS without aliasing caused by non-uniform spatial sampling: Algorithm, validation and illustration. *Journal of Atmospheric and Solar-Terrestrial Physics*, 105400. https://doi.org/10.1016/j.jastp.2020.105400

Savastano, G., Komjathy, A., Verkhoglyadova, O., Mazzoni, A., Crespi, M., Wei, Y., & Mannucci, A. J. 2017. Real-Time Detection of Tsunami Ionospheric Disturbances with a Stand-Alone GNSS Receiver: A Preliminary Feasibility Demonstration. Scientific Reports, 7, 46607. https://doi.org/10.1038/srep46607

Thomas, D., Bagiya, M. S., Sunil, P. S., Rolland, L., Sunil, A. S., Mikesell, T. D., et al., 2018. Revelation of early detection of co-seismic ionospheric perturbations in GPS-TEC from realistic modelling approach: Case study. Scientific Reports, 8(1), 1–10. https://doi.org/10.1038/s41598-018-30476-9

Tsugawa, T., Saito, A., Otsuka, Y., Nishioka, M., Maruyama, T., Kato, H., & Murata, K. T., 2011. Ionospheric disturbances detected by GPS total electron content observation after the 2011 off the Pacific coast of Tohoku Earthquake. Earth, planets and space, 63(7), 66.

UNISDR, C. 2015. The human cost of natural disasters: A global perspective.

Vijayan, M. S. M., G. Varghese, and K. Shimna., 2013. IONODETECT: A software to compute Ionospheric TEC perturbations using dual frequency geodetic GPS data, CSIR C-MMACS Annual Report 2012–2013, pp. 77–78. http://csir4pi.in/images/20132013_annual.pdf

Wang, X., & Liu, P. L. F., 2006. An analysis of 2004 Sumatra earthquake fault plane mechanisms and Indian Ocean tsunami. Journal of Hydraulic Research, 44(2), 147-154.